Quaternary Science Reviews 326 (2024) 108476

Contents lists available at ScienceDirect

Quaternary Science Reviews

journal homepage: www.elsevier.com/locate/quascirev

The >250-kyr Lake Chala record: A tephrostratotype correlating archaeological, palaeoenvironmental and volcanic sequences across eastern Africa

Catherine Martin-Jones [a,b], Christine S. Lane [a,c,*], Maarten Blaauw [d], Darren F. Mark [e,f], Dirk Verschuren [b], Thijs Van der Meeren [b], Maarten Van Daele [g], Hannah Wynton [a], Nick Blegen [a,h], Mary Kisaka [i,j], Melanie J. Leng [k,l], Philip Barker [m]

[a] Department of Geography, University of Cambridge, UK
[b] Limnology Unit, Department of Biology, Ghent University, Ghent, Belgium
[c] Research Laboratory for Archaeology and the History of Art, University of Oxford, Oxford, UK
[d] ^{14}CHRONO Centre, Archaeology and Palaeoecology, School of Natural and Built Environment, Queen's University Belfast, Belfast, UK
[e] Scottish Universities Environmental Research Centre, East Kilbride, G75 0QF, UK
[f] School of Earth & Environmental Earth Sciences, University of St Andrews, St Andrews, KY16 9TS, UK
[g] Renard Centre of Marine Geology, Department of Geology, Ghent University, Ghent, Belgium
[h] Texas A&M University–San Antonio, Department of Mathematical, Physical & Engineering Sciences, USA
[i] College of Earth Sciences, University of Dodoma, Tanzania
[j] Department of Geography, Vrije Universiteit Brussel, Belgium
[k] British Geological Survey, Keyworth, Nottingham, NG12 5GG, UK
[l] School of Biosciences, University of Nottingham, UK
[m] Lancaster Environment Centre, University of Lancaster, UK

ARTICLE INFO

Handling editor: Giovanni Zanchetta

Keywords:
Pleistocene
Holocene
East African rift system
Africa
Palaeoclimate
Lake sediments
Tephrochronology
Geochronology
Argon-dating
Geochemistry
Lake Chala

ABSTRACT

Regional tephrostratigraphic frameworks connect palaeoclimate, archaeological and volcanological records preserved in soils or lake sediments via shared volcanic ash (tephra) layers. In eastern Africa, tracing of tephra isochrons between geoarchaeological sequences is an established chronostratigraphic approach. However, to date, few long tephra records exist from sites with continuous depositional sequences, such as lake sediments, which offer the potential to connect local and discontinuous sequences at the regional scale. Long lake sediment sequences may also capture more complete eruptive histories of understudied volcanic centres. Here, we present and date the tephrostratigraphic record of a >250,000-year (>250-kyr) continuous sediment sequence extracted from Lake Chala, a crater lake on the Kenya-Tanzania border near Mt Kilimanjaro. Single-grain glass major and minor element analyses of visible and six cryptotephra layers reveal compositions ranging from mafic foidites and basanites to more evolved tephri-phonolites, phonolites, trachytes and a single rhyolite. Of these, nine are correlated to scoria cone eruptions of neighbouring Mt Kilimanjaro or the Chyulu volcanic field ~60 km to the north; seven are correlated to phonolitic eruptions of Mt Meru, ~100 km to the west; and four to voluminous trachytic eruptions of Central Kenyan Rift (CKR) volcanoes located ~350 km to the north. The only rhyolitic tephra layer, a cryptotephra, correlates to the 73.7-ka BP (before present, taken as 1950 CE) Younger Toba Tuff (YTT) from Sumatra. Two of the CKR tephra layers provide direct ties with terrestrial sequences relevant to Middle Stone Age archaeology of the eastern Lake Victoria basin in Kenya. Absolute age estimates obtained by direct ^{40}Ar/^{39}Ar dating of 10 tephra layers are combined with six ^{210}Pb and 162 ^{14}C dates covering the last 25-kyr and the well-constrained known age of the YTT to build a first absolute chronology for the full Lake Chala sediment sequence. The uninterrupted >250-kyr Lake Chala sedimentary archive represents a unique tephrostratotype sequence for eastern Africa, optimising the chronological value of tephra correlations in regional palaeoenvironmental, archaeological and volcanological research. Further study of cryptotephra in the Lake Chala sequence and additional geochemical characterisation and dating of ancient volcanic eruptions from

* Corresponding author. Department of Geography, University of Cambridge, Downing Place, Cambridge, CB3 2EN, UK.
E-mail address: csl44@cam.ac.uk (C.S. Lane).

https://doi.org/10.1016/j.quascirev.2023.108476
Received 7 August 2023; Received in revised form 16 December 2023; Accepted 17 December 2023
Available online 20 January 2024

nearby and further afield may eventually produce a regionally connected and detailed tephrostratigraphic framework for eastern equatorial Africa.

1. Introduction

Voluminous explosive volcanic eruptions may inject large volumes of volcanic ash (tephra) into the atmosphere, where it may then be widely distributed and deposited back onto the Earth's surface (Rose and Durant, 2009). Tephra blanketing a downwind landscape in the hours to days following the eruption may be permanently preserved in a variety of depositional environments, from lake-bottom sediments to terrestrial soil sequences, over hundreds or even thousands of kilometres distant from the volcano (Jensen et al., 2014; van der Bilt et al., 2017; Smith et al., 2018). Owing to the rapid dispersal and deposition of tephra layers, they can be used as time markers and, if sufficiently widespread and physically and chemically distinct, they can provide the all-important chronological links allowing the correlation and integration of disparate sedimentary archives (Davies, 2015; Ponomareva et al., 2015; Lane et al., 2017). Ideally, the compilation of sequences of inter-bedded tephra layers across a large study region produces a robust stratigraphic and chronological framework in which regional palaeoenvironmental and archaeological events can be synchronised and dated (Lowe et al., 2015; Davies et al., 2016). In volcanically active regions with high-quality sedimentary settings, tephra deposits can also provide a record of the tempo of past eruptions (Rawson et al., 2015; McNamara et al., 2018; Ortega-Guerrero et al., 2018) that may be used to explore the likelihood and possible scale and impacts of future eruptions. A notable advance in the field of tephrochronology during the last two decades has been the finding and identification of so-called *crypto*-tephra layers, which represent far travelled volcanic ash and are so thin and fine-grained that they cannot be visually discerned from their host sediments. Cryptotephra studies greatly increase the opportunities for tephra correlation over large distances and across wide areas, thereby enhancing our ability to date palaeoenvironmental and archaeological records as well as to reconstruct detailed eruptive histories (Dugmore, 1989; Turney et al., 1997; Lane et al., 2014, 2017; Davies, 2015).

In the volcanically active region of the East African Rift System (EARS), tracing tephra isochrons between geoarchaeological sequences (e.g. Blegen et al., 2021) is starting to provide a common stratigraphic framework for Early, Middle and Late Stone Age deposits, together encompassing the last ~3.3 Ma. However, even though detailed work has been carried out on individual volcanic systems (e.g. Fontijn et al., 2012; Kisaka et al., 2021; Tadesse et al., 2022), the geochemical datasets and eruptive histories for many of the sub-continent's volcanic centres are incomplete, so that the true potential of tephra layers to correlate between distant palaeoenvironmental archives and associated archaeological sites remains unfulfilled.

As an important step towards realisation of this potential, the present study aims to establish a reference tephrostratotype sequence for eastern equatorial Africa, as has previously been done in areas of Europe, for example, where the ~130-kyr long tephrostratigraphy of Lago Grande di Monticchio provides a tephrostratotype for Italian volcanism spanning back to the last interglacial (Wulf et al., 2004, 2008, 2012; Lowe et al., 2015). Here this goal is pursued by comprehensive geochemical documentation and dating of visible tephra layers contained in the >250-kyr long, depositionally continuous sediment sequence of Lake Chala, a deep crater lake near Mt. Kilimanjaro, extracted by the International Continental Scientific Drilling Program (ICDP) project DeepCHALLA (Verschuren et al., 2013; Maitituerdi et al., 2022). Our data add a chronologically well-constrained >250-kyr long record of regional volcanic eruptions to the growing number of studies using terrestrial soil sequences and/or lake-sediment records to document Mid-Pleistocene to Holocene volcanic activity in the EARS (Olago et al., 2000; Poppe et al., 2016; Fontijn et al., 2010, 2018; Martin-Jones et al., 2017; Lane et al., 2018; McNamara et al., 2018; Blegen et al., 2021; Kisaka et al., 2021). We demonstrate the value of the DeepCHALLA record as tephrostratotype for eastern equatorial Africa by examining tephra correlations between Lake Chala and terrestrial outcrops in the eastern Lake Victoria basin (ELVB; ~450 km to the west) and the Central Kenyan Rift valley (CKR; ~350 km to the north).

1.1. The East African Rift System

The volcanically and tectonically active EARS stretches ~2200 km from Ethiopia's Afar Triple Junction southwards through Kenya and Tanzania to northern Mozambique. Volcanism in the EARS was initiated in northern Kenya around 45 Ma BP (Macgregor, 2015) and later spread through much of eastern Africa, forming hundreds of volcanoes, many of which experienced caldera-forming eruptions well into the Quaternary (Macdonald et al., 1987; Scott and Skilling, 1999; Hutchison et al., 2016; Fontijn et al., 2018). A significant number of these volcanic centres have shown continued unrest (Biggs et al., 2009, 2011), but comparatively little data exist on the timing and frequency of past eruptions (Global Volcanism Program, 2023).

The EARS is an ideal location to apply tephrochronology to an array of palaeoenvironmental and archaeological questions (Pyle, 1999; Olago et al., 2000). Complex regional climate dynamics interact with spatially variable rift topography to foster a broad mosaic of environments and landscapes that modern humans and their extinct relatives have inhabited throughout the ~7 Myr of hominin evolution. Rifting processes, including rapid sedimentation and therefore burial, followed by uplift, have provided the conditions necessary for preservation and exposure of diagnostic stone tools and fossil remains, many of which are interbedded with widespread tephra deposits (e.g. Katoh et al., 2000; Brown and Fuller, 2008; McHenry, 2012; Balashova et al., 2016; McHenry and Stanistreet, 2018). Tephra deposits studied in relation to the palaeoanthropological record have linked sites of important fossil finds in Ethiopia, Kenya, Tanzania and Uganda (Brown et al., 1992; Brown and Fuller, 2008; Feibel, 1999; Pickford et al., 1991; Wolde-Gabriel et al., 2005), and consequently have been instrumental in unravelling the rate of anatomical and behavioural changes throughout human evolution. However, the tephra record of the Middle (~780–126 ka BP) to Late Pleistocene (~126–11.7 ka BP), a key period for determining the chronology and conditions of modern human evolution as well as the dispersal of early modern humans beyond Africa, has only recently begun to attract adequate attention (e.g., Blegen et al., 2015, 2016, 2021).

1.2. The sediment record of Lake Chala as potential tephrostratotype for eastern Africa

Lake Chala (3.3° S; 37.7° E; also written 'Challa' after the nearby village) is located at ~880 m elevation on the border between Kenya and Tanzania immediately southeast of Mt. Kilimanjaro. It fills a steep-sided volcanic caldera basin which likely formed during Mt. Kilimanjaro's most recent phase of activity, previously dated by Nonnotte et al. (2008) to 200-150 ka BP. Lake Chala has a surface area of 4.2 km^2, a maximum water depth varying between 92 and 98 m (1999–2017), and is maintained against a negative local water balance by subsurface inflows originating from rainfall onto the forested and subalpine slopes of Mt. Kilimanjaro (Bodé et al., 2020). The lower water column of Lake Chala is permanently stratified and anoxic (Buckles et al., 2014), promoting undisturbed accumulation of finely laminated diatomaceous organic sediments (Verschuren et al., 2009; Wolff et al., 2011, 2014) interrupted

only by turbidites and tephra layers (Verschuren et al., 2013; Van Daele et al., 2017; Baxter et al., 2023).

A first set of overlapping sediment cores from Lake Chala, extracted by the CHALLACEA project in 2003 and 2005, yielded diverse insights in the climate and environmental history of easternmost equatorial Africa spanning the last 25 kyr (e.g., Verschuren et al., 2009; Barker et al., 2011; Damsté et al., 2011, 2012; van Geel et al., 2011; Nelson et al., 2012; Meyer et al., 2018), as well as detailed reconstruction of climate variability and climate-human-landscape interaction within the last two millennia (Buckles et al., 2016; van der Plas et al., 2021). Based on

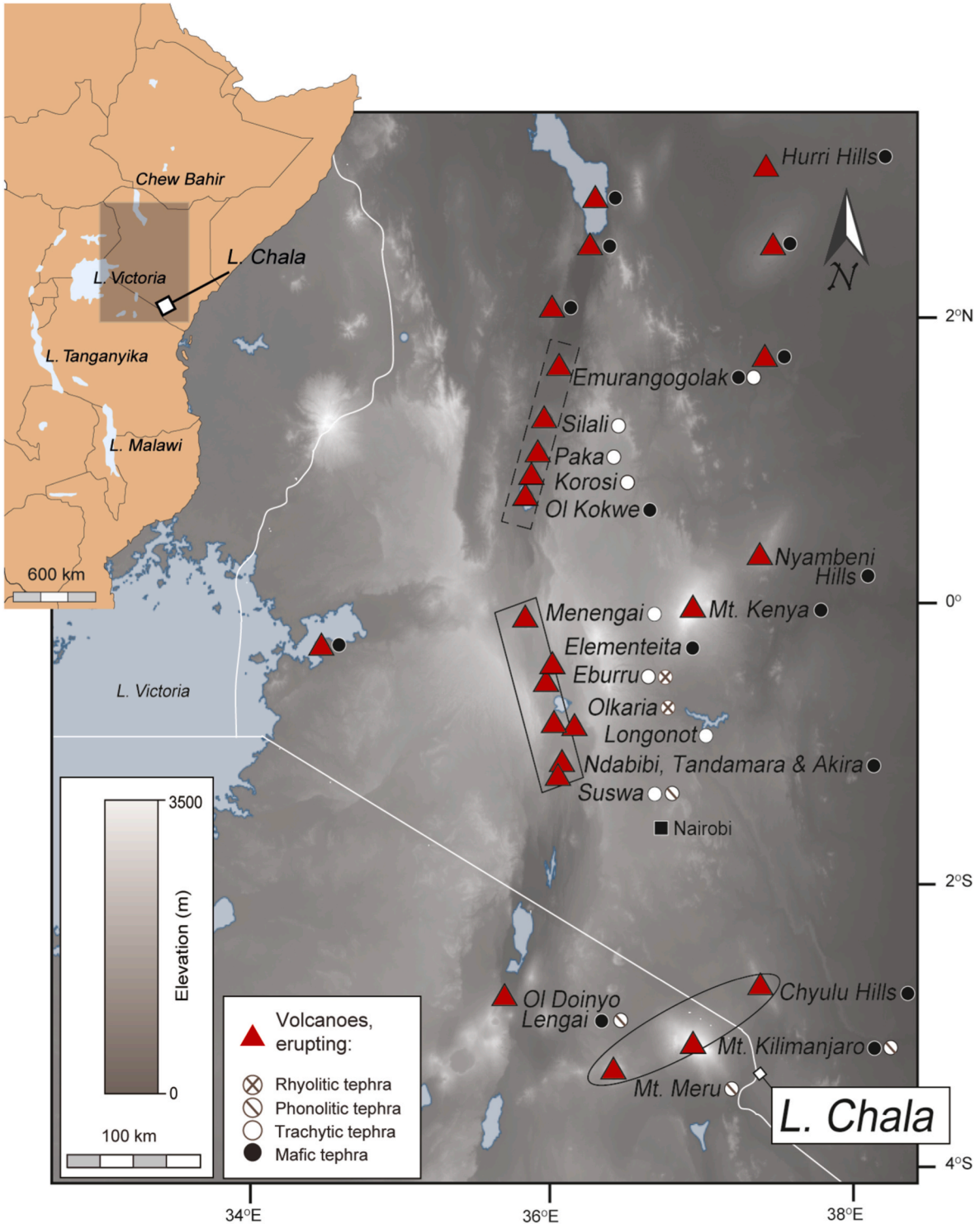

Fig. 1. Location of Lake Chala in relation to volcanic centres in the eastern branch of the East African Rift System (EARS), thought to have been active during the Middle to Late Pleistocene. These include volcanoes in the Central Kenyan Rift (dashed box = northern set, solid line box = southern set, after Williams (1978) and Baker (1987)), off-Rift locations (black ellipse) and northern Tanzania. Circular symbols indicate the typical composition of pyroclastic units erupted from each volcanic centre, recognising that some have erupted variable compositions through time. Map data sources: DEM SRTM 30 m elevation models from RCRMD Open Data, overlain with water bodies from the WWF Global Lakes and Wetlands Database and Holocene volcanoes from the Volcanoes of the World database, compiled by the Global Volcanism Program (2023). Maps rendered in QGIS.

analysis of high-resolution seismic reflection data penetrating the entire sedimentary infill and extrapolation of the basal age of the radiocarbon-dated CHALLACEA sequence, Moernaut et al. (2010) estimated that the ~210 m thick infill of lacustrine sediments in Lake Chala represents (near-) continuous deep-water sediment accumulation over the last ~250 kyr (Verschuren et al., 2013). In November 2016, drilling by the DeepCHALLA project at an offshore location above the eastern depocenter of the Chala crater basin recovered a composite sediment sequence reaching 214.8 m below the lake floor (214.8 mblf), shortly penetrating the lowermost seismic reflector that was believed to represent the base of the lacustrine deposits (Moernaut et al., 2010). High-resolution line-scan images acquired immediately after core splitting at the National Lacustrine Core Facility of the University of Minnesota (Minneapolis, USA) allowed cross-correlation with mm-scale precision between overlapping 3-m core sections recovered from adjacent holes at the drill site, producing a single composite sediment sequence with 100% recovery in the uppermost 133 m and ~85% recovery in the lower part. Detailed re-analysis of the seismic profiles that intersected with the DeepCHALLA drill site confirmed depositional continuity throughout the recovered sediment sequence (Maitituerdi et al., 2022), in line with the total absence of lithological disconformities, erosional surfaces or evidence of subaerial exposure in the recovered sediment sequence. Being entirely composed of fine-grained, finely laminated to banded diatomaceous lake muds, the Lake Chala sedimentary archive is therefore expected to produce palaeoclimate and palaeoenvironmental reconstructions of unparalleled detail for eastern equatorial Africa (e.g., Baxter et al., 2023). Dating of the tephra horizons contained in this record is key to construction of a robust absolute chronology for those reconstructions. As it also provides a continuous, high-fidelity record of regional volcanic activity, we here explore its potential to become an important tephrostratotype sequence for equatorial eastern Africa.

1.3. Explosive volcanism in the EARS

The tephra layers in Lake Chala sediments most likely originate from volcanoes in the Kenyan and Tanzanian sections of the EARS, many of which are evidenced to have been active during the Middle to Late Pleistocene timeframe covered by the DeepCHALLA sequence. Based on location, volcanoes in the study area can be divided in two groups (Fig. 1), namely those associated with the main axis of the eastern branch of the EARS in Kenya and northern Tanzania ('Rift volcanoes'; section 1.3.1), and off-axis volcanoes located on the shoulders of the EARS ('Off-Rift volcanoes'; section 1.3.2.).

1.3.1. Rift volcanoes

As defined by Williams (1978) and Baker (1987), Rift volcanoes in Kenya can be divided into a northern and a southern set. Explosive phases of the northern set (Emuruangogolak, Silali, Korosi, Paka and Ol Kokwe) have erupted large volumes of mildly alkaline to transitional basalt with lesser trachytes (Williams, 1978). Emuruangogolak began erupting pantelleritic trachytes as well as basalts ~1 Ma ago (Weaver, 1977). The Silali trachytic shield volcano has a 5–8 km summit caldera which formed ~63 ka BP (Macdonald et al., 1995). Prior to that, Silali erupted trachytic tuffs between ~135 and 123 ka BP (Tryon et al., 2008). Tephra deposits within the Kapthurin Formation in the Lake Baringo basin are geochemically correlated to proximal deposits of the nearby Korosi volcano, which reveal Korosi began erupting both trachytic and basaltic tephra ~396 ka BP (Blegen et al., 2018). The Paka volcano erupted large volumes of trachytic pyroclastics since ~390 ka BP, with a caldera collapse ~38 ka BP and post-caldera activity continuing into the Holocene (Dunkley et al., 1993; Mibei et al., 2021).

Volcanoes in the southern section of the Kenyan Rift (Menengai, Eburru, Olkaria, Longonot and Suswa) are characterised by explosive eruptions (Williams, 1978; Macdonald et al., 1987) and some have deposited widespread tephra layers. The 36 ka BP Menengai Tuff, for example, has been traced across >115,000 km^2 of Kenya (Blegen et al., 2016).

The rhyolitic compositions of the Eburru and Olkaria volcanic complexes are unique in Kenya, providing the tephra layers with particularly recognisable fingerprints. Lane et al. (2018) described peralkaline rhyolitic tephra layers in Holocene lake sediments from Lake Victoria, and linked them geochemically to the Eburru and Olkaria volcanoes, demonstrating westward ash transport exceeding 250 km.

Further south, Longonot is a relatively young trachytic stratovolcano rising inside the remnants of an 8 × 12 km caldera that formed around ~21 ka BP. Since then it has known several explosive eruptions generating deposits of airfall pumice (Scott and Skilling, 1999). Suswa, the southernmost volcano in the Kenyan Rift, has erupted abundant trachytic-phonolitic lavas and tuffs between ~240 and 100 ka BP (Scott and Skilling, 1999; White et al., 2012). Minor basalts, basaltic-trachyandesites and trachyandesites have also erupted from the Ndabidi, Tandamara and Elementeita lava fields situated adjacent to the Eburru, Olkaria and Suswa calderas (White et al., 2012). Basaltic ash cones at Elmenteita, the youngest of these fields, have been suggested to post-date the Early-to Mid-Holocene high-stand of Lake Naivasha (Thompson and Dodson, 1963; Richardson and Richardson, 1972).

Volcanic activity associated with the EARS continues into northern Tanzania, where Ol Doinyo Lengai is the only volcano known to have erupted natrocarbonatite in historical times (Dawson et al., 1995). At Engare Sero on the south shore of Lake Natron, natrocarbonatite tephras erupted from Ol Doinyo Lengai preserved human footprints of Early Holocene age (Balashova et al., 2016). The bulk of the volcano is, however, made up of phonolitic and nephelenitic units which have been correlated to a series of ~400–15 ka BP tuffs, as well as the Holocene Namorod Ash outcropping in Olduvai Gorge (Hay, 1989; Bell and Dawson, 1995). Less is known about the Gelai, Ketumbeine and Kerimasi volcanoes and the Lake Natron–Engaruka Monogenetic Volcanic field (LNE-MVF), which lie directly east of Ol Doinyo Lengai. The LNE-MVF hosts ~200 scoria and tuff cones, rings and maars which erupt basanites, melilites and evolved nephelinites and are estimated to be of Late Pleistocene to Holocene age (Dawson and Powell, 1969). In July 2007, a dyke was intruded on the southern flanks of Gelai, signalling that the LNE-MVF is a young, still-active volcanic field (Calais et al., 2008).

1.3.2. Off-rift volcanoes

Eruptions of off-Rift volcanoes in Kenya and northern Tanzania, which include Mt. Kenya, Mt. Kilimanjaro and Mt. Meru, have compositions ranging widely from alkali basalts to nephelinites and phonolites (Wilkinson et al., 1986; Olago et al., 2000; Späth et al., 2000, 2001; Roberts, 2003; Nonnotte et al., 2008, 2011; Kisaka et al., 2021). The Mt. Kenya volcanic complex erupted basalts and trachytes through the Pliocene and into the Pleistocene (Baker, 1967). The edifice of Mt. Meru is dominated by phonolitic-nephelinitic lavas and pyroclastic deposits attesting to a long history of explosive eruptions (Wilkinson et al., 1986; Roberts, 2003; Kisaka et al., 2021). While volcanism in the wider Meru complex began as early as 1.5 Ma BP, the oldest pyroclastic deposits on the main edifice are estimated to date from between 160 and 110 ka BP (Wilkinson et al., 1986). Interbedded nephelinite volcaniclastic breccias, tuffs and lava flows forming Mt. Meru's summit group have been dated to between ~80 and 60 ka BP (Wilkinson et al., 1986). Kisaka et al. (2021) studied the youngest phase of explosive activity at Meru, as represented by three explosive tephriphonolitic to phonolitic eruptions depositing pumice and ash up to 30 km to the west. The youngest and largest of these (MX3) has an estimated minimum eruption volume of 2.7 km^3.

Radiocarbon dating of associated palaeosols at multiple sites is inconsistent but suggests that these three eruptions of Mt. Meru may have occurred between 40 and 30 ka BP (Kisaka et al., 2021). Further, ~9 ka BP a large-scale sector collapse occurred, generating an avalanche deposit of debris travelling north and east until it reached the slopes of

Mt. Kilimanjaro (Wilkinson et al., 1986; Delcamp et al., 2017). This collapse had previously been associated with the above-mentioned pyroclastic units to the west of Mt. Meru (Wilkinson et al., 1986; Roberts, 2003), but Kisaka et al. (2021) and Delcamp et al. (2017) observed no eruptive products within the debris deposit.

Mt. Kilimanjaro is characterised by three central craters, of which the youngest (Kibo) formed ~1 Ma BP and is characterised by polyphase activity since ~0.5 Ma BP (Nonnotte et al., 2008). Between ~270 and 170 ka BP volcanism from the Kibo vent was dominated by effusion of phonolitic lavas. A 200-m wide 'ash pit' has since developed inside Kibo crater, but no historic eruptions have been recorded (Nonnotte et al., 2008, 2011) and no Holocene events have been confirmed (Global Volcanism Program, 2023). Contemporaneous with the final stages of edification at Kibo, hundreds of parasitic scoria cones, associated with basaltic lavas and minor pyroclastics, have developed along fissures on the north-western and south-eastern flanks of Mt. Kilimanjaro (Nonnotte et al., 2008, 2011).

About 60 km to the northeast of Mt. Kilimanjaro, hundreds of scoria cones clustered along fissures on the shoulders of the Rift valley together comprise the Hurri, Nyambeni and Chyulu fields. Eruptions at Chyulu evolved from foiditic to basaltic compositions through time. The youngest cones, Shaitani and Chainu, erupted as recently as the mid-19th century (Saggerson, 1963; Haug and Strecker, 1995; Späth et al., 2000, 2001).

1.3.3. Volcanoes further afield

As explosive volcanism contemporary with the Lake Chala record has occurred along the full length of the EARS, the potential exists to find relatively exotic tephra layers. In the north, calderas of many of Ethiopia's silicic volcanoes were formed by eruptions dated to between ~320 and 100 ka BP, and some of these are associated with widely distributed tephras which could potentially be found as distal layers in the Lake Chala sediments (Hutchison et al., 2016; Tadesse et al., 2022; Vidal et al., 2022). Volcanoes in the western branch of the EARS, to the west of Lake Victoria, are a less probable source of tephra in Lake Chala due to their typical effusive or only moderately explosive eruptions (Rosenthal et al., 2009) as well as the region's prevailing easterly wind direction.

Tephra produced in voluminous super-eruptions have the potential to be transported many 1000s of kilometres (e.g., Pyle et al., 2006; Shane et al., 1995; Vandergoes et al., 2013) and may provide an exotic source for (crypto-)tephra layers in African lake sediments. A cryptotephra layer deriving from the 73.7 ka BP Younger Toba Tuff (YTT) super-eruption of the Toba caldera in Sumatra (Mark et al., 2014, 2017) has been found in Lake Chala sediments (Baxter et al., 2023); compositional and textural data are included here for comparison with tephra from eastern African volcanoes. The discovery of YTT in Lake Chala adds to previous reports of YTT on the African continent, including in Lake Malawi (Lane et al., 2013) and southern Africa (Smith et al., 2018). Further, the established $^{39}Ar/^{40}Ar$ age of the YTT (73.7 ± 0.6 ka BP) provides a robust isochron for dating the DeepCHALLA sequence.

1.4. Tephra compositional data

Distal tephra layers can often be traced back to the volcano from which they originated by comparing their glass composition with a reference dataset of proximal pyroclastic deposits from regional volcanoes (e.g., Tomlinson et al., 2015). Still, even compositionally distinctive tephra layers can be correlated to specific eruption events only when comparable glass (ash or pumice) analyses are available from the pertinent unit within that proximal stratigraphic record. Historically, much of the published compositional data of proximal EARS volcanic deposits involved whole-rock compositions, which contain variable quantities of phenocrysts and therefore are difficult to precisely compare with glass data from distal tephra deposits. Moreover, limited sampling of proximal volcanic sequences means that published data may not represent the full suite of compositions erupted from a volcano, both within and between eruptions. However, the recent increase of tephrostratigraphic studies in eastern Africa means that more proximal glass analyses are becoming available, and new compilations of tephra compositional data, for example the East African Rift Tephra Database (EARThD) (DiMaggio et al., 2021), facilitate rapid data mining.

2. Methods

2.1. Tephrostratigraphy

Visible tephra layers in Lake Chala sediments were located through detailed visual inspection of the freshly split core sections, already before the overlapping sections were cross-correlated to assemble the composite DeepCHALLA sediment sequence. The exact position of each visible tephra layer in the DeepCHALLA sequence is given a unique ICDP-prescribed code composed of the core section code and the exact depth of the tephra in that core section (Table 1). Due to sediment expansion following the release of hydrostatic pressure during core recovery, the composite DeepCHALLA sediment sequence has a total length of 229.15 mcd (metre composite depth), i.e. ~7% longer than the drilled depth of 214.8 mblf (Maitituerdi, 2023). The depth of all tephra and cryptotephra layers identified in the Lake Chala record is expressed in meter composite depth (mcd; Table 1), as this is the most practical depth scale to use during sub-sampling for palaeoenvironmental reconstruction. Values of composite depth correct for recovery gaps and drilling-related artefacts, but still include the thicknesses of event deposits such as turbidites and tephra layers.

Macroscopically visible tephras were recorded and their constituent glass shards and mineral assemblages examined under high-powered microscopy (100x - 200x magnification) before samples were collected from the full thickness of each tephra for geochemical analysis and dating. Glass shards within each tephra layer were concentrated for geochemical analysis by sieving to retain the >25 μm fraction and separated from lighter sediment components using a sodium polytungstate solution with density of 1.95 g/cm^3.

Cryptotephra investigations reported here were carried out at select depth intervals in the 25-kyr CHALLACEA sequence as part of a pilot study to explore the occurrence and distribution of cryptotephra in Lake Chala sediments. Magnetic susceptibility (MS) and X-ray fluorescence (XRF) scanning data from the CHALLACEA sequence (Kristen, 2009) were used to identify horizons suspected to contain high concentrations of glass shards, as identified by high MS values coinciding with peaks in Fe, K, Zr and Nb (Fig. S1). To assess the presence of cryptotephra, sediments were processed by adapting the non-destructive density floatation methods of Blockley et al. (2005). Samples were extracted from the core as contiguous 10-cm long strips of mud. After sieving to retain the >25 μm fraction and density separation to isolate the particles with density >1.95 g/cm^3, recovered glass shards were permanently mounted on microscope slides in Canada Balsam, for scanning and counting under high-powered microscopy (100x - 200x magnification). All 10-cm depth intervals with abundant glass shards were re-sampled at 1-cm resolution. These samples were processed as before, resulting in a series of shard counts allowing to identify peaks in shard abundance marking the exact position of the primary tephra layer.

Re-inspection of the CHALLACEA sediment sequence after discovery of cryptotephra layers, using the above approach, revealed that four of the seven CHALLACEA cryptotephra are in fact visible in the lithostratigraphy, but had previously gone unnoticed because of sediment disturbance associated with hammer-driven piston coring (Van Daele et al., 2017). Correlations between all visible CHALLACEA and DeepCHALLA tephra layers were confirmed using both the precise transfer of depth scales from the former to the latter core sequence by cross-correlation of mm-scale lamination and agreement between the respective tephra glass shard compositions (Fig. S2). Cryptotephra analysis in the DeepCHALLA sequence has thus far been limited to a targeted search for the 73.7 ka BP YTT (Mark et al., 2014, 2017), in the

Table 1
List of 29 visible tephra and 6 cryptotephra ("crypto.") layers detected to date in the CHALLACEA and DeepCHALLA sequences (*reported in Martin-Jones et al., 2020; †reported in Baxter et al., 2023), with IDs based on their respective composite depth values (mcd), core section and section depth of each tephra layer's basal contact, and corresponding event-free composite depth values (mefd) in the DeepCHALLA sequence. Also indicated: tephra layer thickness, particle appearances and maximum size of the glass shards present (measured as longest axis length). See Table S1 for an expanded version including laboratory sample codes (CT-) and information on crystal content and sizes.

Tephra ID	Core section	Core section depth (cm)	Tephra thickness (cm)	DCH depth (mefd)	Glass shard appearance	Glass shard longest axis length (μm)
					Colour, primary + secondary descriptors: major component; minor component.	
CHALLACEA						
CH-1.18	03-2 Kb	17.5	crypto.	1.528	Colourless, highly vesicular + microlite-rich	<100
CH-2.29 DCH-2.95	03-2Kc	41.7	0.2	2.938	Light brown, blocky + vesicular + microlite-rich	<100
CH-3.51	2 P II	28.4	crypto.	4.379	Light brown, blocky + microlite rich	<100
CH-3.68	2 P II	45.4	crypto.	4.616	Brown, blocky + vesicular	<100
CH-7.64 DCH-9.31	3PIII	171.5	0.5	8.496	Colourless-light brown, blocky + microlites	<100
CH-13.22	3 PV	104.6	crypto.	14.275	Brown, blocky + vesicular	<200
CH-19.29 DCH-22.27	4PVII	36.5	0.2	21.000	Colourless, highly vesicular, rounded + fluted; trace brown	<100
CH-19.35	4PVII	47.2	crypto.	21.102	Colourless, highly vesicular, rounded + fluted; trace brown	<200
DeepCHALLA						
DCH-2.95 CH-2.29	1B–1H-2	20.5	0.3	2.938	Colourless-light brown, highly vesicular + microlite-rich; blocky	<200
DCH-9.31 CH-7.64	1A-4H-3	84.2	1.0	8.496	Colourless, highly vesicular + elongated vesicles	<150
DCH-22.27 CH-19.29	1B–7H-1	127.3	0.5	21.000	Colourless, platy + vesicular; microcryst-rich	<200
DCH-53.90	1B–17H-1	39.7	0.9	49.183	Colourless, platy + vesicular; microcryst-rich	<250
DCH-55.62	1B–17H-3	65.2	1.1	50.837	Colourless, platy; glass-selvedges on crystal-clusters	<200
DCH-56.00	1B–17H-3	103.0	0.8	51.202	Colourless, platy + fluted	<200
DCH-57.60	1B–18H-2	56.7	0.2	52.755	Dark brown, blocky + cuspate, highly vesicular	<1000
DCH-58.03	1B–18H-2	100.2	0.4	53.186	Dark brown, blocky + highly vesicular; frothy	<1000
DCH-58.41	1B–18H-3	21.7	0.2	53.534	Dark + light brown, blocky + fluted; some frothy and altered	<1000
DCH-67.55	1B–21H-2	45.5	crypto.	62.361	Colourless, platy + cuspate; rare fluted	<130
DCH-67.56	1B–21H-2	47.2	0.1	62.377	Colourless, platy; glass-selvedges on crystal-clusters	<400
DCH-69.24	1A-23H-2	23.4	0.3	63.892	Dark brown, blocky; highly vesicular	<100
DCH-72.96	1B–23H-1	12.6	0.4	67.604	Colourless, platy + cuspate	<150
DCH-75.34	1B–23H-3	32.9	0.5	69.978	Colourless, highly vesicular	<100
DCH-75.53	1B–23H-3	52.0	0.3	70.166	Dark brown, vesicular + microlite rich	<250
DCH-75.63	1B–23H-3	62.8	0.9	70.265	Colourless, platy; glass-selvedges on crystal-clusters	<100
DCH-75.91	1A-25H-1	100.0	0.2	70.538	Colourless, platy; glass-selvedges on crystal-clusters	<100
DCH-79.46	1B–25H-1	16.5	0.5	74.082	Colourless, platy; glass-selvedges on crystal-clusters	<250
DCH-88.02	1A-29H-1	34.2	2.0	82.622	colourless/beige, blocky; elongated/fluted	<350
DCH-98.76	1B–31H-1	21.3	0.3	93.341	Colourless, platy; glass-selvedges on crystal-clusters	<350
DCH-105.40	1B–33H-1	44.8	0.3	99.662	Colourless, platy; glass-selvedges on crystal-clusters	<250
DCH-111.72	1B–35H-1	33.8	0.3	104.997	Light brown, platy; vesicular + microlites	<600
DCH-117.70	1C-3E-2	145.9	0.6	110.278	Colourless, platy; glass-selvedges on crystal-clusters	<400
DCH-121.60	1A-40H-1	27.4	1.5	113.879	Colourless, blocky + cuspate + vesicular	<150
DCH-128.70	1C-7E-2	84.7	0.1	119.502	Light brown, platy	<350
DCH-143.55	1D-3E-1	55.2	0.2	130.760	Colourless, platy; glass-selvedges on crystal-clusters	<200
DCH-144.21	1D-3E-1	120.6	0.2	131.269	Colourless, platy; glass-selvedges on crystal-clusters	<500
DCH-173.85	1D-12E-2	9.4	0.3	155.826	Colourless, platy; glass-selvedges on crystal-clusters	<200
DCH-175.83	1E-23E-2	106.4	3.0	157.123	Colourless-beige, platy + blocky; fluted + vesicular	<500
DCH-228.60	1E-45E-3	122.5	0.9	190.188	Brown, blocky + microlite rich; vesicular	<1000

1.9-m interval between 65.9 and 67.8 mcd as guided by the preliminary, age-depth model for the complete DeepCHALLA sequence developed by Martin-Jones et al. (2020); we refer to Baxter et al. (2023) for details.

For convenient reference, each tephra layer was assigned a unique code referring to either the CHALLACEA (CH-) or DeepCHALLA (DCH-) sequence from which it was extracted and the composite depth (in mcd) of its basal contact, following Martin-Jones et al. (2020). This system is maintained even when tephra layers have been correlated between the two sequences, using both labels when compositions are combined for comparison to reference data. The composite depth values of all tephra layers were then converted to the DeepCHALLA event-free composite depth scale (mefd; Maitituerdi, 2023) in which the thicknesses of event deposits (turbidites ≥0.5 cm and all tephra layers) are excluded with the purpose to produce an absolutely dated age-depth model (Section 2.2.2) limited to the conformably deposited primary lacustrine muds. The thickness of all visible tephra layers is presented here; turbidite thicknesses were inventoried by Swai (2018).

2.2. Tephrochronology

2.2.1. $^{40}Ar/^{39}Ar$ dating

Considering that the majority of visible tephra layers in the DeepCHALLA sequence are thin (Table 1: average thickness 0.6 cm), the sample volume available for $^{40}Ar/^{39}Ar$ dating was maximised by extracting all 29 visible tephra layers in their entirety from the sediment record (combining working and archive halves of the master sequence, and cross-correlated 'off-splice' sections where available). This effort yielded samples of nearly pure tephra ranging between ~10 and 100 g wet weight.

Sample preparation followed Mark et al. (2017). Feldspars (sanidine)

were separated by manual disaggregation of samples, washing and sieving followed by magnetic and density separations and finally ultrasonic cleaning in 5% hydrofluoric acid for 5 min. Feldspar crystals (63–400 μm) were finally handpicked under a binocular microscope for analysis and at this point, 11 of the 29 samples were deemed to contain sufficient crystals to be targeted for $^{40}Ar/^{39}Ar$ dating. Samples were irradiated in the CLICIT facility of the Oregon State University TRIGA reactor using the Alder Creek (AC) sanidine (Nomade et al., 2005) as neutron fluence monitor. $^{40}Ar/^{39}Ar$ analyses were then conducted at the National Environmental Isotope Facility, Scottish Universities Environmental Research Centre.

The age (t) of a primary ashfall tephra sample is given by the equation $t = \lambda^{-1} \ln(J \times R+1)$ with λ the radioactive decay constant of ^{40}K ($5.463 \pm 0.107 \times 10^{-10}$ yr^{-1}), J a parameter relating to the fluence of the neutron bombardment during irradiation, and R the $^{40}Ar^*/^{39}Ar$ ratio. For J determinations, standard positions bracketing each unknown were used to monitor the neutron fluence. Ten measurements were made for each bracketing standard position. The weighted average $^{40}Ar^*/^{39}Ar_K$ was calculated for each well, and the arithmetic mean and standard deviation of these three values were used to characterize the neutron fluence for the unknowns. This approach was deemed sufficient as, due to the relatively short duration of irradiations, there was no significant variation between the positions in a single level of the irradiation holder (a 16-well pan, with all samples co-irradiated). No data were rejected for all J measurements. Irradiation durations and J measurements are provided in Tables S5–S6.

Samples were analysed by total fusion with a CO_2 laser, and measurements made using an ARGUS VI noble gas mass spectrometer, equipped with a Nier-type ion source, 10^{12} Ohm amplifiers on the ^{40}Ar to ^{37}Ar channels, and a digital CDD electron multiplier detector on the ^{36}Ar channel. All 10 samples were analysed in a single batch. For backgrounds and mass discrimination measurements (via automated analysis of multiple air pipettes, run on average after every three analyses) see Tables S5–S6. Backgrounds subtracted from ion beam measurements were arithmetic means and standard deviations. Mass discrimination was computed based on a power law relationship (Renne et al., 2009) using the isotopic composition of atmospheric Ar reported by Lee et al. (2006) and independently confirmed by Mark et al. (2011). Corrections for radioactive decay of ^{39}Ar and ^{37}Ar were made using the decay constants reported by, respectively, Stoenner et al. (1965) and Renne and Norman (2001). Ingrowth of ^{36}Ar from the decay of ^{36}Cl, corrected using the $^{36}Cl/^{38}Cl$ production ratio and methods of Renne et al. (2008), was determined to be negligible. Argon isotope data corrected for backgrounds, mass discrimination, and radioactive decay and ingrowth are given in Table S4.

Ages were computed from the blank-, discrimination- and decay-corrected Ar isotope data after additional correction for interfering isotopes based on the following production ratios, determined from fluorite and Fe-doped $KAlSiO_4$ glass: $(^{36}Ar/^{37}Ar)_{Ca} = (2.650 \pm 0.022) \times 10^{-4}$; $(^{38}Ar/^{37}Ar)_{Ca} = (1.96 \pm 0.08) \times 10^{-5}$; $(^{39}Ar/^{37}Ar)_{Ca} = (6.95 \pm 0.09) \times 10^{-4}$; $(^{40}Ar/^{39}Ar)_K = (7.3 \pm 0.9) \times 10^{-4}$; $(^{38}Ar/^{39}Ar)_K = (1.215 \pm 0.003) \times 10^{-2}$; $(^{37}Ar/^{39}Ar)_K = (2.24 \pm 0.16) \times 10^{-4}$, as determined previously for this reactor in the same irradiation conditions (Renne et al., 2008). Ages and their uncertainties are based on the methods of Renne et al. (2010), the calibration of the decay constant reported by Renne et al. (2011) and the optimised AC sanidine age of 1.1891 ± 0.0008 Ma as reported by Niespolo et al. (2017).

For some of the age comparisons made in this paper, contributions from sources of systematic uncertainty (i.e., in the $^{40}Ar/^{40}K$ of the standard and ^{40}K decay constants) are neglected and only analytical uncertainties in isotope measurements of samples and standards are included. These uncertainties are herein referred to as the 'analytical precision'. For the purposes of this study, analytical uncertainties include contributions from uncertainties in the interference corrections because these interference corrections have variable effects due to the slightly variable chemistry of the analysed samples.

Outliers in single-crystal samples were discriminated using a 3-sigma filter applied iteratively until all samples counted are within 3 standard deviations of the weighted average ± one standard error. This procedure screened for older crystals that might logically be interpreted as xenocrysts. No younger outliers were recorded during analysis of any samples. Processing of the data using the *n*MAD approach of Kuiper et al. (2008) had no impact on the probability distribution plots for each sample. Sample-specific isotope correlation plots and ideograms are presented in Table S7.

2.2.2. Age-depth modelling

To produce age estimates for all tephra layers identified in this study we constructed a Bayesian age-depth model using BACON (Blaauw and Christen, 2011) for the complete DeepCHALLA sediment sequence, which we herein refer to as DCH_TephraAge. This age-depth model combines all ^{14}C and ^{210}Pb ages that could be securely transferred from the 25-kyr CHALLACEA sequence (Verschuren et al., 2009; Blaauw et al., 2011) with the 10 $^{40}Ar/^{39}Ar$ age estimates based on direct dating of DeepCHALLA tephras (this study) and the imported age of the YTT (73.7 ± 0.6 ka) found at 67.55 mcd (62.361 mefd) (Baxter et al., 2023).

Transfer of the CHALLACEA age model to the DeepCHALLA sequence was done through cross-correlation of mm-scale lamination shared between the two sediment sequences, which were recovered from sites located ~600 m apart but both within the lake's modern profundal depositional area (Maitituerdi et al., 2022). This procedure provided 162 ^{14}C and 6 ^{210}Pb ages to 168 exact depth intervals in the uppermost 23.3 m of the DeepCHALLA sequence, and pin-pointed the depth of the CHALLACEA sediment-water interface (2005 CE) in the DeepCHALLA sequence recovered 11 years later. Due to coring artefacts suffered by the CHALLACEA sequence (Wolff et al., 2011; Van Daele et al., 2017), 25 other ^{14}C-dated depth intervals could not be correlated with sufficient precision to the DeepCHALLA stratigraphy, and were omitted from the construction of DCH_TephraAge. Considering the equatorial location of Lake Chala, the transferred Challacea ^{14}C dates were calibrated using a 1:1 mix of the northern and southern hemisphere calibrations IntCal20 (Reimer et al., 2020) and SHCal20 (Hogg et al., 2020), adding 10 years of uncertainty to account for uncertainties regarding the mixing balance, and using old-carbon age offsets for ^{14}C dates on bulk organic matter as previously determined by Blaauw et al. (2011). Age extrapolation below the lowermost absolutely dated depth interval (tephra DCH-175.83, see below) was constrained by setting the accumulation prior mean to 1540 year m-1, based on a long-term mean accumulation rate of 0.65 m kyr-1 between DCH-53.90 (at 49.183 mefd) and DCH-175.83 (at 157.153 mefd). Section widths were set at 0.25 m, and all other settings were kept at their defaults.

2.3. Tephra geochemistry

All CHALLACEA and DeepCHALLA tephra (Table 1) were prepared and analysed for major and minor element composition using wavelength-dispersive electron probe microanalysis (WDS-EPMA) following methods outlined in Martin-Jones et al. (2020). No new trace element data has been produced within the scope of this study. However, DCH-67.55 (YTT) and all mafic tephras in the Lake Chala record have been analysed previously to determine their trace element compositions using laser ablation inductively coupled mass spectrometry, with results presented in Martin-Jones et al. (2020) and (Baxter et al., 2023).

Single grain glass shard analysis for most tephra layers was carried out using a wavelength-dispersive Cameca SX100 electron microprobe (WDS-EPMA) at the Department of Earth Sciences, University of Cambridge. Eight CHALLACEA cryptotephra were analysed on a JEOL8600 WDS-EPMA at the Research Laboratory for Archaeology and the History of Art, University of Oxford (Table S9). Both instruments were run with a 10-μm diameter defocussed beam with a 15 kV accelerating voltage and 6 nA beam current. Sodium was collected first and for 10 s, P for 60 s and

all other elements for 30 s. The instruments were calibrated against a series of mineral standards and analyses were quantified using the PAP absorption correction method. Assays of the MPI-DING standards KL2-G (basalt) and St-Hs6/80-G (andesite) (Jochum et al., 2005, 2006) and an in-house Lipari obsidian (peralkaline rhyolite) standard were used to test the calibration and monitor accuracy across the two instruments. EPMA datasets were checked for any analyses that targeted accidental (non-glass shard) grains or where the beam area encapsulated microlites or epoxy resin. Hits with analytical totals <94% by weight, or distinct compositional outliers, were discarded from further data analysis (more subtle outliers are retained and noted as such in Table S9). All major element data presented in the main text, tables and figures are normalised to 100% to account for variable secondary hydration of glasses.

2.4. Correlating tephra layers to source volcanoes

Where possible, we compared Lake Chala tephra glass compositions to published glass data from other distal deposits or from proximal volcanic sources. The comparisons were made using multiple combinations of major and minor element bi-plots and visual assessment of similarity. Limited availability of glass geochemical reference datasets for eruptions from EARS volcanic centres, and the limited data acquired from some of the Chala tephra layers, precludes a discriminative statistical approach (Lowe et al., 2017; Bolton et al., 2020). Primary samples of potentially correlative tephra deposits from Mt Meru, available to the authors, were reanalysed alongside the Chala tephra, using identical analytical conditions to minimise the possibility of miscorrelation due to instrumental differences (Table S10).

For those volcanic centres and eruptive events from which no or only limited glass compositional data were available for comparison, we drew broad comparisons between tephra glass and available whole-rock compositions and differentiated between volcanic centres using combinations of major and minor element bi-plots. Chronostratigraphic evidence was used to guide correlation of Lake Chala tephras to candidate eruption events, when available. Correlations established in this study, particularly those based on whole-rock data or incomplete proximal datasets, should be seen as working hypotheses that may be tested as more detailed comparative data become available.

3. Results

3.1. Lake Chala tephrostratigraphy

The Lake Chala record contains 29 visible tephra layers ranging in thickness from 0.1 to 3 cm, and to date six cryptotephra layers have been detected and analysed (Table 1, Fig. S1). Guided by bracketing sections of mm-scale laminated matrix sediments, three visible tephra layers could be traced between the overlapping sections of the CHALLACEA and DeepCHALLA cores, and this cross-correlation was confirmed using glass geochemistry: CH-2.29 corresponds to DCH-2.95, CH7.64 to DCH-9.31, and CH-19.29 to DCH-22.27 (Fig. S2). Martin-Jones et al. (2020) described seven of the visible tephras, containing light to dark brown scoriaceous shards with occasional ropey Pele's hair type fragments <1000 μm in length. The other 22 visible tephras have colourless to beige glass shards, typically <500 μm in length (Table 1, Fig. 2). Many of these tephra are composed of vesicular, crystal-free shards, however, 12 layers contain frequent clusters of crystals covered in a veneer of clear glass, alongside varying proportions of clear, bubble wall-type shards.

Of the six cryptotephra layers detected to date, five were found in the CHALLACEA sequence (Table 1, Fig. S1). CH-13.22 and CH-3.68 contain brown scoriaceous glass in concentrations of 98 shards/g dry sediment and 6887 shards/g dry sediment, respectively (Martin-Jones et al., 2020). The three other CHALLACEA cryptotephra layers contain clear to light-brown glass shards with varied morphologies, from highly vesicular to blocky shards, with some microlites (Table 1), suggesting intermediate to evolved glass compositions.

Cryptotephra layer DCH-67.55 was identified as a pronounced peak of ~300,000 shards/g dry sediment located at 45–45.5 cm depth in section DCH-1B-21-H-2 of the DeepCHALLA sequence (Baxter et al., 2023). Tephra shards are clear and platy, making them morphologically distinct from those in all other Lake Chala tephra layers observed to date (Fig. 2).

3.2. Tephrochronology

3.2.1. $^{40}Ar/^{39}Ar$ dating results

Of the 11 tephra samples processed for $^{40}Ar/^{39}Ar$ dating one sample (DCH-2.95) failed to produce an age, partly due to the small (<100 μm) size of its constituent crystals and partly due to the low yields of radiogenic ^{40}Ar associated with a high amount of atmospheric Ar contamination, likely related to alteration. The 10 other samples defined coherent juvenile populations (Table S7) and returned two-sigma age uncertainties ranging from ±0.3% to ± 28% (Table 2). The results for DCH-75.34 displayed in Fig. 3 illustrate data quality and statistical robustness. Sample age precision was a function of crystal size, K content and atmospheric Ar contamination, which controlled how much radiogenic ^{40}Ar was available for mass spectrometer measurement. Casting all data of this sample (Table S7) on an isotope correlation plot (Fig. 3a) defines ages that are indistinguishable from ideogram juvenile population ages, and initial trapped components indistinguishable from the modern-day atmosphere (Lee et al., 2006; Mark et al., 2011).

3.2.2. Tephra-based age-model

DCH_TephraAge is the first age model for the full Lake Chala sediment record, as drilled by the DeepCHALLA project, based on absolute age constraints (Fig. 4; Table S8). Extending the published 25-kyr CHALLACEA age model (Blaauw et al., 2011) throughout the DeepCHALLA sequence, it shows good agreement with preliminary age models based on extrapolation of the 25-kyr CHALLACEA sequence and seismic-stratigraphic links between the DeepCHALLA and CHALLACEA sites (Moernaut et al., 2010; Verschuren et al., 2013; Martin-Jones et al., 2020). The most divergence with these earlier age models is the basal age of the DeepCHALLA sediment sequence, which DCH_TephraAge estimated as dating to 266 -±7 ka BP (Table S8), while the earlier (extrapolated) age models had predicted it to be around 250 ka BP.

Constrained by prior settings on sedimentation time and memory, DCH_TephraAge adheres closely to the CHALLACEA age model for the last 25-kyr constructed by Blaauw et al. (2011), and partly bypasses three of the 10 $^{40}Ar/^{39}Ar$ ages on Lake Chala tephras (Fig. 4). Two of these dated tephras (DCH-22.27 and DCH-88.02) exert little guidance to the local age-depth relationship because of their relatively large age uncertainties (±2.9 ka and ±3.1 ka; Table 2); DCH-67.56 is bypassed because of its very close position to the YTT, of which the absolute age is both more precisely constrained (±0.6 ka versus ±0.9 ka) and more consistent with long-term mean accumulation (Fig. 4). Two other Lake Chala tephras with large age uncertainties (DCH-9.31 and DCH-121.60) also exert little age-model guidance but are consistent either with adjacent ^{14}C-dated intervals (DCH-9.31) or long-term mean accumulation (DCH-121.60; Fig. 4). Taking the modelled ages as refinements on individual $^{40}Ar/^{39}Ar$ age estimates, we follow DCH_TephraAge to assign absolute ages and associated age uncertainties to each of the 35 Lake Chala tephra layers (Table 3), thereby updating the provisional ages of seven tephras analysed earlier by Martin-Jones et al. (2020) and dated using an extrapolated age model.

3.3. Tephra compositions

Table 3 summarises major and minor element glass compositions of 32 of the 35 sampled CHALLACEA and DeepCHALLA tephra layers. No pure glass EPMA measurements were achieved on DCH-117.70, DCH-121.60 and DCH-144.21, which contained very few glass shards. Similarly, due to high microlite content, the few analyses (n ≤ 3) on DCH-

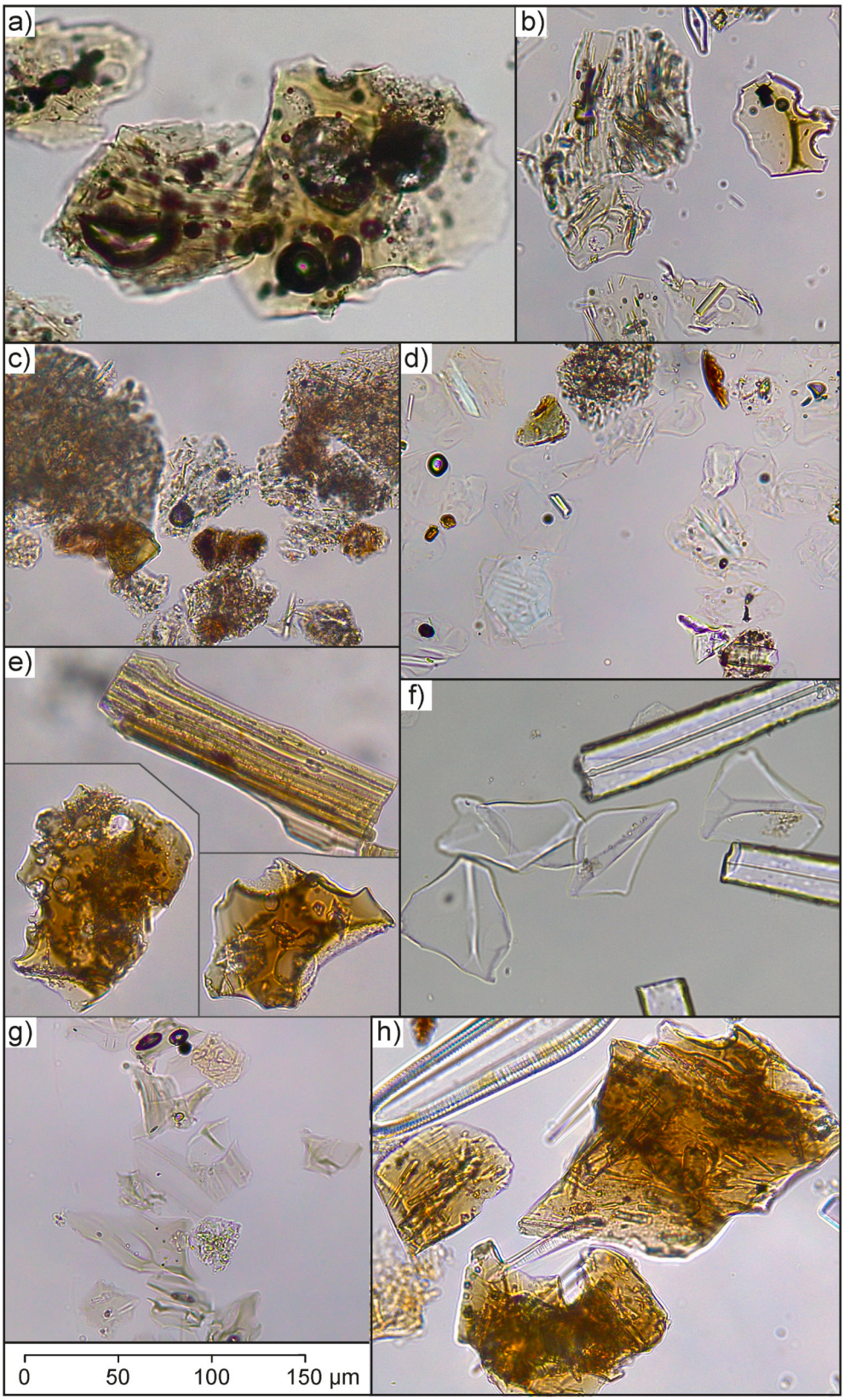

Fig. 2. Photomicrographs of selected tephra shards extracted from Lake Chala sediments, representing the morphological variation observed within and between samples (Table 1). a) CH-2.29 and b) CH-19.29 show common light brown, blocky or stretched, often vesicular shards ± microlites; c) DCH-55.62 provides an example of rounded clusters of crystals, with trace free glass; d) DCH-56.00 is mainly composed of colourless, platy shards, with few microlites and some crystal clusters; e) examples of brown, blocky and fluted shards from DCH 58.81 and DCH-69.24; f) DCH-67.55 contains clear, platy and tri-cuspate shards, entirely microlite free (rod-like particles are sponge-spicules); g) DCH-175.83 is composed of beige, platy, cuspate and fluted shards, few with vesicles; h) DCH-228.60 contains brown, blocky, microlite rich shards. Images taken in plane polarised light using a Leica DMP-750 microscope, at ×400 magnification, then reduced to fit page. The scale bar in (g) applies to all images.

75.63 and DCH-143.55 show divergent compositions and are omitted from data comparisons (e.g., Fig. 5). Based on major element biplots (Fig. 5), glass compositions of the CHALLACEA and DeepCHALLA tephras can be divided in three distinct groups.

- Among 11 phonolitic tephra, CH1.18, DCH-53.90, DCH-56.00, DCH-79.46, DCH-98.76, DCH-105.40 and DCH-173.85 plot closely together and as a relatively discrete population on nearly all elemental bi-plots (Figs. 5 and 7), suggesting a common source.
- Two of the three youngest tephra layers, DCH-2.95/CH-2.29 and CH-

Table 2
Summary of $^{40}Ar/^{39}Ar$ data. Full results are presented in Tables S4–7.

Tephra ID	$^{40}Ar/^{39}Ar$ Age (ka)	±2σ (ka, analytical)	±2σ (ka, full)	MSWD	Prob.	Crystals
DCH-9.31	9.45	2.00	2.04	0.6	0.8	13
DCH-22.27	25.33	2.90	2.89	0.6	0.9	15
DCH-53.90	49.03	1.10	1.12	1.8	0.1	10
DCH-67.56	77.01	0.92	0.93	0.8	0.6	14
DCH-75.34	83.69	0.72	0.74	1.3	0.2	13
DCH-88.02	93.94	3.10	3.15	0.5	0.9	13
DCH-105.40	126.16	0.97	0.98	1.4	0.2	13
DCH-121.60	146.50	2.30	2.27	1.4	0.2	10
DCH-143.55	169.64	0.57	0.58	1.8	0.04	14
DCH-175.83	215.17	0.61	0.63	1.5	0.1	15

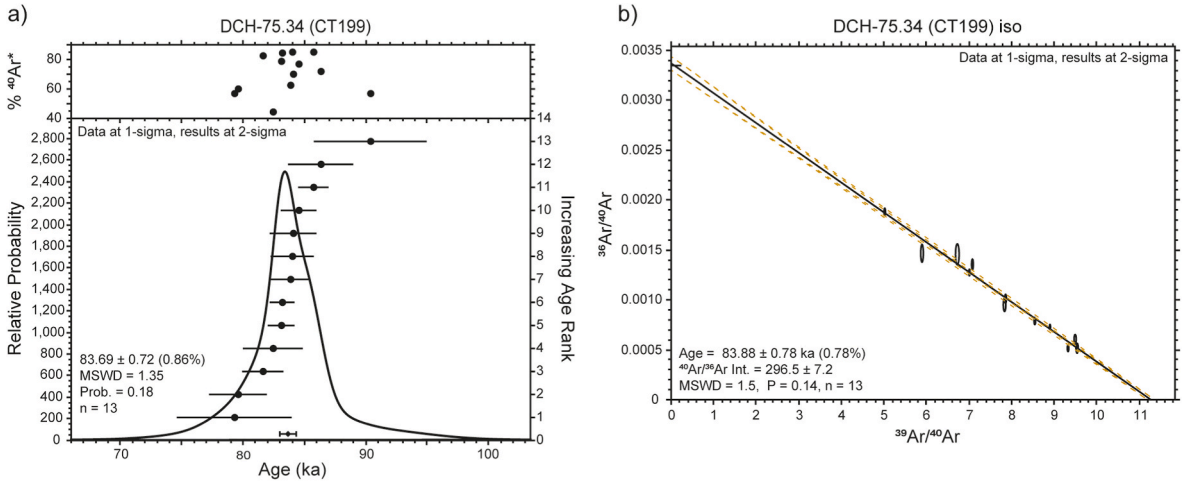

Fig. 3. $^{40}Ar/^{39}Ar$ ideogram (a), and isotope correlation plot (b), defining the population age for DCH-74.34. Only analytical uncertainties are shown, see Table 2 for sample uncertainties including full external precision, and Table S7 for equivalent plots on all $^{40}Ar/^{39}Ar$ -dated tephra samples.

3.3.1. *Mafic tephras (<50 wt % SiO_2)*

As described by Martin-Jones et al. (2020), seven visible tephra layers (DCH-57.60, DCH-58.03, DCH-58.41, DCH-69.24, DCH-75.53, DCH-111.72 and DCH-228.60) and two cryptotephra (CH-3.68, CH-13.22) in the Lake Chala sequence have a mafic composition. Besides the low (<50 wt %) SiO_2 content, these tephra have glass compositions characterised by 13–16 wt % Al_2O_3, 11–14 wt % FeOt and <11 wt % total alkalis (Fig. 5).

3.3.2. *Intermediate tephras (50–70 wt% SiO_2)*

The majority of Lake Chala tephras (n = 19) have compositions spanning the tephriphonolite, phonolitic and trachytic fields on element bi-plots (Fig. 5). While many of these compositions overlap, some tephra have a more distinctive uni- or bimodal major and minor element composition, and similarities between two or more tephra suggest that they derive from common source volcanoes. For example.

- Tephras DCH-72.96, DCH-88.02, DCH-128.70 and DCH-175.83 span the phonolite-trachyte boundary and are depleted in Al_2O_3 and enriched in FeOt relative to other Lake Chala tephras with similar SiO_2 and alkali element concentrations (Figs. 5 and 6).

3.51, are tephriphonolites which can be distinguished from the main cluster of intermediate tephra based on slightly lower SiO_2 compositions (<56 wt %) and higher FeOt (>4 wt %) (Fig. 5).

Some intermediate tephra (e.g., DCH-75.34) vary by as much as 5 wt % in both silica and total alkali concentrations (Fig. 5), while others display large variation in other element oxides as evidenced by standard deviations in Table 3 (e.g., DCH-9.31/CH-7.64: mean CaO = 2.26 ± 0.98 wt %). Much of this variation in individual element oxides may result from the difficulty of isolating pure-glass analytes from crystal-rich shards with limited glass veneers. In addition, real geochemical trends and multi-modal tephra (e.g., DCH-22.27, DCH-75.34, DCH-75.91 and DCH-128.70) inherently display high standard deviations. These factors are most apparent in those tephras from which only a small number of glass shard analyses could be acquired (e.g., DCH-75.34, n = 8; DCH-75.63, n = 4; DCH-143.55, n = 3). We refer to the raw data in Table S8 to further explore possible drivers of relatively high element oxide variability in particular samples.

3.3.3. *Rhyolitic tephra (>75 wt% SiO_2)*

As reported in Baxter et al. (2023), cryptotephra DCH-67.55 is compositionally unique among the tephra layers in the Lake Chala

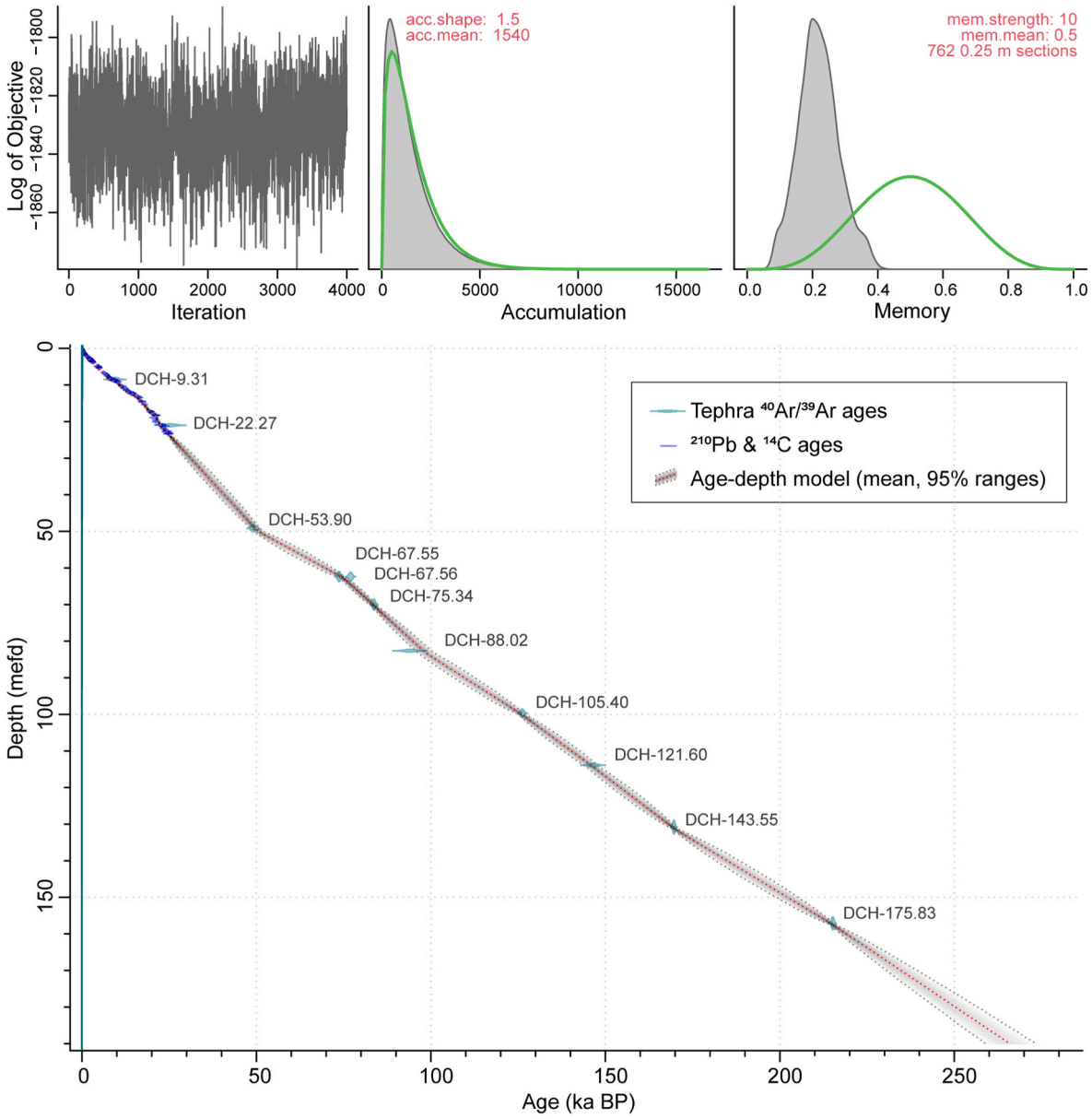

Fig. 4. Output of the Bayesian DCH_TephraAge age-depth model, run in BACON (Blaauw and Christen, 2011) (Table S8). a) Markov chain Monte Carlo (MCMC) run, b) prior (grey) and posterior (green) distributions for accumulation rate, c) Memory settings, prescribing the variability in accumulation rate, and d) age-depth model, constrained by ^{210}Pb, ^{14}C and ^{40}Ar/^{39}Ar ages estimates plotted with 95% (two-sigma) confidence ranges and codes for the ^{40}Ar/^{39}Ar-dated tephra samples added for reference. Lacking datable tephra near the base of the sequence, the age model extrapolates 33 mefd beyond the deepest ^{40}Ar/^{39}Ar age estimate at 157.123 mefd; see Discussion.

sequence. The glass shards of DCH-67.55 contain higher SiO_2 (>75 wt %) and lower Al_2O_3 (12–13 wt %) and FeOt (~1 wt %) than all other Lake Chala tephras analysed to date as well as all other (peralkaline) rhyolites known to have erupted from Kenyan and Ethiopian volcanoes (Fig. 5).

3.4. Correlating Lake Chala tephra to volcanic sources and regional tephra layers

The multiple physical and chemical distinctions among the Lake Chala tephras hint to varied volcanic eruptive processes and origins within and beyond the EARS. Below we detail some of the more secure tephra source correlations, before noting some yet unknown sources calling for further work.

3.4.1. Mafic tephras: correlation to Mt. Kilimanjaro and Chyulu Hills scoria cones

Martin-Jones et al. (2020) previously correlated the two oldest of nine mafic Lake Chala tephras (DCH-111.72 and DCH-228.60) to scoria-cone eruptions from the flanks of neighbouring Mt. Kilimanjaro, and the seven younger ones (CH-3.68, CH-13.22, DCH-57.60, DCH-58.03, DCH-58.41, DCH-69.24 and DCH-75.53) to the Chyulu Hills scoria cone field, ~60 km to the north of Lake Chala (Fig. 1). These correlations were based on similarities in glass composition, including incompatible trace element ratios, to published whole rock compositions from Mt. Kilimanjaro and Chyulu Hills (Späth et al., 2000; Nonnotte et al., 2011). Mt. Kilimanjaro and the Chyulu Hills are the volcanoes closest to Lake Chala that are known to have erupted mafic tephras within the ~265-ka timeframe of its sediment record (Fig. 1). However, Kisaka et al. (2021) report more than 120 mafic scoria cones in the region surrounding Mt. Meru, ~100 km to the west of Lake Chala,

Table 3
Average major and minor element glass compositions of CHALLACEA (CH-) and DeepCHALLA (DCH-) tephra layers, with standard deviations (±2σ) and normalised to 100% anhydrous totals. For tephra layers with distinct bi-modal compositions, separate averages for each mode are denoted a-b. Raw data and secondary standards are provided in Tables S9–11. DCH_TephraAge age estimates are the modelled 95% confidence ranges for each tephra in ka BP, rounded to nearest 10 years; mean and median values are provided in Table S1.

		n	SiO2	TiO2	Al2O3	FeO	MnO	MgO	CaO	Na2O	K2O	P2O5	*DCH_TephraAge*
			weight %										*mean (ka BP)*
CH-1.18	Avg.	*7*	55.14	0.60	20.18	4.51	0.20	0.28	1.60	11.18	6.26	0.06	*0.74–0.45*
	±2 σ		*1.02*	*0.10*	*1.41*	*0.88*	*0.10*	*0.17*	*0.63*	*1.11*	*0.73*	*0.03*	
DCH-2.95/CH-2.29a	Avg.	*21*	52.14	1.84	20.22	6.13	0.17	1.65	4.04	8.65	4.75	0.41	*2.27–1.85*
	±2 σ		*0.47*	*0.13*	*0.28*	*0.30*	*0.03*	*0.13*	*0.29*	*0.22*	*0.17*	*0.04*	
DCH-2.95/CH-2.29b	Avg.	*11*	54.67	1.85	20.36	6.22	0.17	1.59	4.03	5.84	4.84	0.43	
	±2 σ		*0.89*	*0.16*	*0.34*	*0.33*	*0.03*	*0.17*	*0.39*	*0.51*	*0.15*	*0.04*	
CH-3.51	Avg.	*22*	53.25	1.67	19.98	6.16	0.17	1.58	3.74	8.32	4.72	0.41	*3.90–3.16*
	±2 σ		*1.16*	*0.38*	*0.77*	*0.79*	*0.10*	*0.45*	*0.93*	*0.73*	*0.43*	*0.13*	
CH-3.68	Avg.	*34*	45.24	4.28	14.29	13.44	0.21	5.41	11.06	3.72	1.54	0.79	*4.10–3.32*
	±2 σ		*1.14*	*0.16*	*0.57*	*1.00*	*0.08*	*0.58*	*0.35*	*0.39*	*0.10*	*0.11*	
DCH-9.31/CH-7.64	Avg.	*11*	54.97	0.94	21.51	4.15	0.17	0.50	2.26	9.97	5.41	0.12	*8.22–7.31*
	±2 σ		*1.36*	*0.44*	*1.13*	*0.91*	*0.09*	*0.33*	*0.98*	*0.91*	*0.61*	*0.15*	
CH-13.22	Avg.	*5*	46.48	4.33	14.59	12.52	0.17	5.17	10.74	3.53	1.70	0.77	*17.17–16.32*
	±2 σ		*1.81*	*0.28*	*1.13*	*1.45*	*0.12*	*1.76*	*2.11*	*1.23*	*0.65*	*0.31*	
DCH-22.27/CH-19.29a	Avg.	*13*	52.79	0.98	21.21	5.00	0.17	0.55	2.53	10.43	6.20	0.14	*22.94–22.25*
	±2 σ		*0.69*	*0.09*	*0.39*	*0.24*	*0.07*	*0.09*	*0.37*	*0.80*	*0.44*	*0.23*	
DCH-22.27/CH-19.29b	Avg.	*5*	55.82	1.04	21.17	5.08	0.18	0.59	2.68	6.85	6.48	0.11	
	±2 σ		*0.74*	*0.07*	*0.43*	*0.17*	*0.07*	*0.14*	*0.30*	*0.41*	*0.12*	*0.04*	
CH-19.35	Avg.	*7*	53.67	0.97	20.57	4.99	0.18	0.51	2.50	10.34	6.18	0.09	*22.99–22.39*
	±2 σ		*1.76*	*0.22*	*2.08*	*1.25*	*0.14*	*0.22*	*0.45*	*0.54*	*0.60*	*0.05*	
DCH-53.90a	Avg.	*8*	56.34	0.57	21.70	3.65	0.15	0.26	1.49	10.55	5.24	0.04	*50.98–48.42*
	±2 σ		*0.14*	*0.02*	*0.16*	*0.09*	*0.04*	*0.02*	*0.06*	*0.17*	*0.12*	*0.01*	
DCH-53.90b	Avg.	6	59.36	0.62	21.79	3.68	0.14	0.22	1.56	7.00	5.57	0.06	
	±2 σ		*0.38*	*0.03*	*0.18*	*0.09*	*0.03*	*0.01*	*0.07*	*0.34*	*0.12*	*0.02*	
DCH-55.62	Avg.	*21*	61.13	0.64	20.41	3.75	0.16	0.34	1.78	6.87	4.82	0.09	*53.98–50.58*
	±2 σ		*1.57*	*0.12*	*0.52*	*0.82*	*0.05*	*0.10*	*0.48*	*1.60*	*0.61*	*0.04*	
DCH-56.00a	Avg.	*10*	57.36	0.42	21.01	3.87	0.21	0.19	1.18	10.21	5.51	0.04	*54.79–51.06*
	±2 σ		*1.09*	*0.05*	*0.55*	*0.27*	*0.06*	*0.02*	*0.09*	*0.59*	*0.23*	*0.03*	
DCH-56.00b	Avg.	*5*	61.79	0.24	20.34	2.12	0.13	0.11	1.03	8.69	5.53	0.03	
	±2 σ		*0.35*	*0.04*	*0.66*	*0.21*	*0.04*	*0.02*	*0.17*	*0.72*	*0.47*	*0.01*	
DCH-57.60	Avg.	*14*	45.00	4.47	15.13	13.33	0.19	5.23	10.64	3.84	1.51	0.67	*58.32–53.52*
	±2 σ		*0.35*	*0.21*	*0.45*	*0.47*	*0.06*	*0.30*	*0.34*	*0.21*	*0.12*	*0.06*	
DCH-58.03	Avg.	*21*	45.16	4.37	15.10	12.90	0.21	4.67	10.55	4.32	1.78	0.94	*59.23–54.23*
	±2 σ		*1.42*	*0.56*	*0.76*	*0.99*	*0.10*	*0.39*	*1.18*	*0.60*	*0.27*	*0.22*	
DCH-58.41	Avg	*27*	45.21	4.43	14.65	12.79	0.22	4.95	11.01	4.06	1.79	0.90	*59.93–54.86*
	±2 σ		*0.57*	*0.15*	*0.32*	*0.69*	*0.10*	*0.41*	*0.34*	*0.50*	*0.14*	*0.09*	
DCH-67.55	Avg	*32*	77.07	0.05	12.54	0.88	0.05	0.06	0.78	3.17	5.38	0.02	*75.09–73.12*
	±2 σ		*0.57*	*0.02*	*0.31*	*0.18*	*0.11*	*0.03*	*0.19*	*0.42*	*0.28*	*0.04*	
DCH-67.56	Avg.	*11*	57.24	1.00	20.77	4.09	0.17	0.63	2.44	8.71	4.82	0.14	*75.11–73.16*
	±2 σ		*0.88*	*0.06*	*0.32*	*0.33*	*0.08*	*0.04*	*0.14*	*0.53*	*0.41*	*0.04*	
DCH-69.24	Avg.	*28*	44.79	4.41	13.75	13.55	0.21	5.87	11.24	3.71	1.69	0.78	*77.41–75.23*
	±2 σ		*0.55*	*0.12*	*0.34*	*0.49*	*0.05*	*0.50*	*0.23*	*0.31*	*0.13*	*0.09*	
DCH-72.96	Avg.	*6*	62.82	0.46	16.96	5.71	0.26	0.24	0.96	8.05	4.49	0.05	*81.87–79.26*
	±2 σ		*0.93*	*0.09*	*0.35*	*0.88*	*0.05*	*0.06*	*0.13*	*0.83*	*0.68*	*0.03*	
DCH-75.34	Avg.	*8*	63.97	3.03	15.82	9.47	0.18	3.22	7.79	5.29	3.35	0.58	*84.15–82.45*
	±2 σ		*4.57*	*4.30*	*5.50*	*11.93*	*0.19*	*4.73*	*10.54*	*3.47*	*4.80*	*0.82*	
DCH-75.53	Avg.	*23*	44.56	4.55	13.81	13.72	0.23	4.97	11.60	4.07	1.63	0.86	*84.32–82.71*
	±2 σ		*0.85*	*0.22*	*1.24*	*1.15*	*0.11*	*0.91*	*1.18*	*0.78*	*0.20*	*0.12*	
DCH-75.63	Avg.	*4*	67.29	0.07	18.09	0.75	0.00	0.06	1.27	6.86	5.59	0.04	*84.45–82.81*
	±2 σ		*2.46*	*0.14*	*4.53*	*1.12*	*0.04*	*0.08*	*2.41*	*4.20*	*5.20*	*0.07*	
DCH-75.91a	Avg.	*3*	61.06	0.30	20.12	3.00	0.17	0.12	1.02	7.73	6.43	0.05	*84.81–83.14*
	±2 σ		*0.59*	*0.05*	*2.22*	*0.26*	*0.04*	*0.01*	*0.19*	*1.99*	*0.36*	*0.04*	
DCH-75.91b	Avg.	*8*	65.86	0.07	19.26	0.89	0.05	0.04	0.79	6.49	6.54	0.02	
	±2 σ		*1.69*	*0.15*	*1.24*	*0.91*	*0.10*	*0.07*	*0.56*	*1.25*	*1.71*	*0.03*	
DCH-79.46	Avg.	*10*	57.72	0.30	21.75	3.11	0.13	0.12	0.92	10.60	5.33	0.02	*89.77–86.47*
	±2 σ		*1.14*	*0.03*	*1.04*	*0.23*	*0.07*	*0.01*	*0.07*	*0.75*	*1.23*	*0.06*	
DCH-88.02	Avg.	*14*	60.70	0.58	15.43	7.77	0.36	0.30	1.07	8.70	5.00	0.10	*100.12–95.66*
	±2 σ		*0.79*	*0.04*	*0.44*	*0.43*	*0.10*	*0.05*	*0.09*	*0.54*	*0.29*	*0.07*	
DCH-98.76	Avg.	*17*	57.55	0.50	21.63	3.35	0.13	0.22	1.30	9.33	5.95	0.05	*117.85–112.32*
	±2 σ		*1.26*	*0.07*	*0.78*	*0.38*	*0.11*	*0.09*	*0.38*	*1.43*	*0.61*	*0.05*	
DCH-105.40	Avg.	*16*	57.52	0.59	21.44	3.65	0.14	0.36	1.70	9.59	5.59	0.09	*126.60–124.34*
	±2 σ		*1.78*	*0.10*	*0.68*	*0.46*	*0.12*	*0.04*	*0.23*	*1.36*	*0.38*	*0.09*	
DCH-111.72	Avg.	*14*	45.94	3.95	15.63	12.26	0.21	4.10	10.11	4.48	2.34	0.98	*135.48–131.04*
	±2 σ		*0.81*	*0.27*	*0.64*	*0.64*	*0.05*	*0.63*	*1.12*	*0.59*	*0.28*	*0.13*	
DCH-128.70a	Avg.	*10*	60.97	0.69	13.91	9.15	0.42	0.37	1.22	8.29	4.89	0.10	*156.15–151.05*
	±2 σ		*0.98*	*0.04*	*0.33*	*0.55*	*0.06*	*0.05*	*0.14*	*0.49*	*0.46*	*0.03*	
DCH-128.70b	Avg.	*9*	64.50	0.73	13.98	9.03	0.43	0.33	1.19	4.53	5.18	0.10	
	±2 σ		*1.35*	*0.04*	*0.39*	*1.04*	*0.08*	*0.06*	*0.20*	*0.62*	*0.36*	*0.07*	
DCH-143.55	Avg.	*3*	64.04	0.17	19.80	2.09	0.15	0.05	0.60	6.50	6.56	0.03	*169.95–168.22*
	±2 σ		*4.73*	*0.11*	*3.58*	*0.93*	*0.16*	*0.03*	*0.78*	*4.25*	*2.68*	*0.05*	

(*continued on next page*)

Table 3 (*continued*)

		n	SiO2	TiO2	Al2O3	FeO	MnO	MgO	CaO	Na2O	K2O	P2O5	*DCH_TephraAge*
			weight %										*mean (ka BP)*
DCH-173.85	Avg.	*10*	55.14	0.58	21.70	3.76	0.15	0.29	1.50	10.97	5.79	0.11	*213.77–210.32*
	±2 σ		*0.45*	*0.03*	*0.40*	*0.25*	*0.08*	*0.05*	*0.20*	*0.73*	*0.22*	*0.12*	
DCH-175.83	Avg.	*12*	60.39	0.58	14.95	8.83	0.40	0.19	1.09	8.91	4.60	0.07	*215.32–213.52*
	±2 σ		*1.25*	*0.08*	*0.69*	*0.95*	*0.12*	*0.05*	*0.15*	*1.46*	*0.29*	*0.06*	
DCH-228.60	Avg.	*25*	44.93	3.36	16.06	11.20	0.26	4.03	9.72	6.17	2.93	1.33	*~266*
	±2 σ		*0.65*	*0.21*	*0.49*	*0.57*	*0.14*	*0.38*	*0.72*	*0.59*	*0.24*	*0.13*	

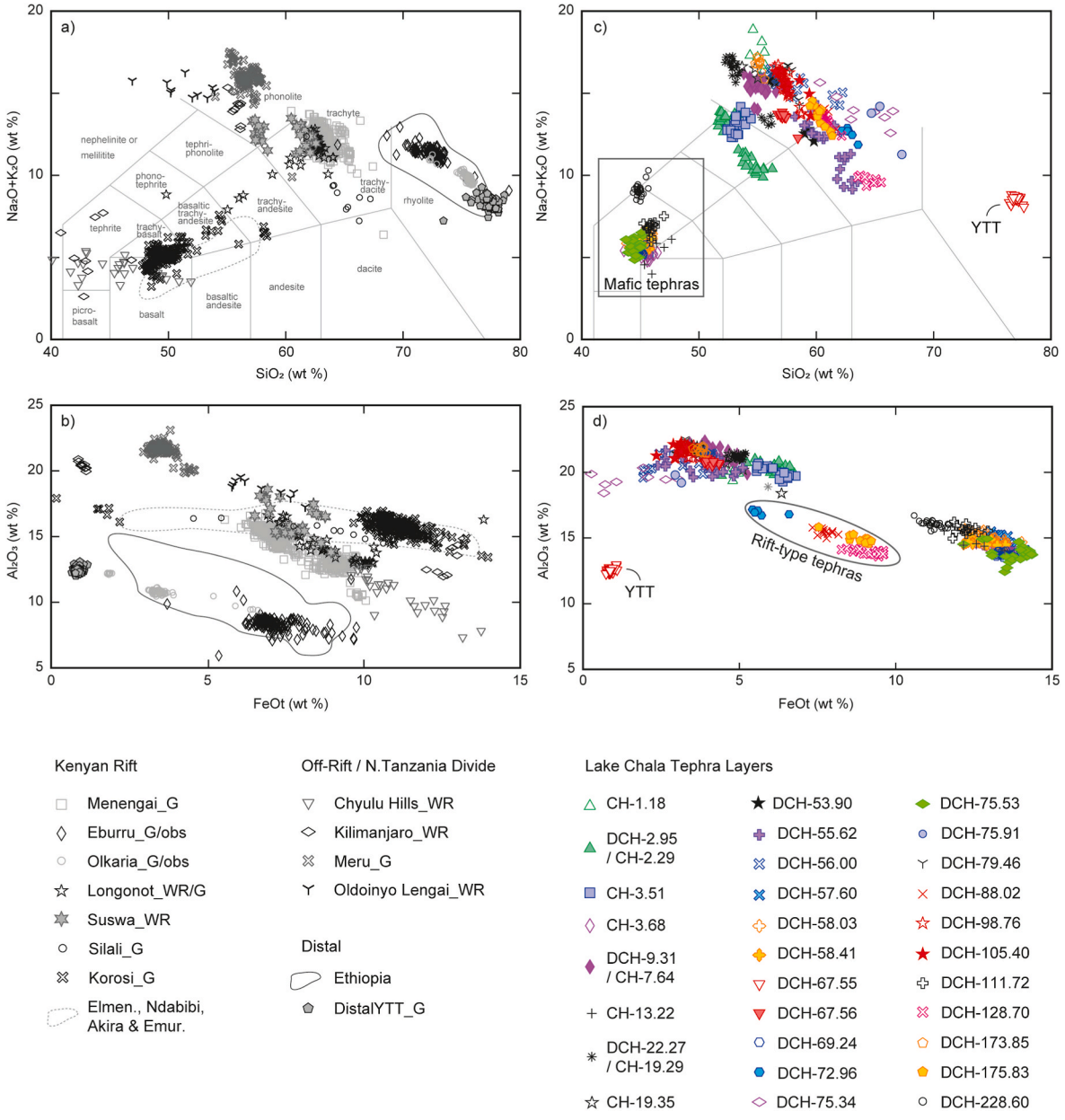

Fig. 5. *Total alkali-silica biplots (Le Bas et al., 1986) of the geochemical compositions of tephra and lava from possible source volcanoes (a-b) and Lake Chala tephras (c-d), including single-grain glass data (G), obsidian data (obs) and whole rock lava and/or pumice samples (WR), as available. (a-b) Compositions of Late Pleistocene Kenyan and Tanzanian eruption products, distal rhyolite tephras from Ethiopia and the Younger Toba Tuff (YTT). The envelope for Elmenteita (Elmen.), Ndabibi, Akira and Emuruangogolak (Emur.) rift basalts and data for Suswa lavas and tuffs are from White et al. (2012); data for Silali are from Tryon et al. (2008); Korosi data are from the Bedded Tuff Member glass (Tryon and McBrearty, 2002, 2006; Blegen et al., 2018); Menengai Tuff data are from Blegen et al. (2016); Eburru obsidian data are from Brown et al. (2013), tephra data from Lane et al. (2018) and Blegen et al. (2021); Olkaria obsidian data are from Brown et al. (2013) and Marshall et al. (2009), tephra data from Lane et al. (2018); Longonot pumice data are from Scott and Skilling (1999), lava data from Rogers et al. (2004); Mt. Meru pumice glass data are from Kisaka et al. (2021) and this study; data on Mt. Kilimanjaro lavas from Nonnotte et al. (2011); and Chyulu Hills data are from Späth et al. (2001). Ol Doinyo Lengai WR lava data from Klaudius and Keller (2006). The envelope for Ethiopian rhyolitic tephra is after Fontijn et al. (2018). Distal YTT data are from Lane et al. (2013), and Smith et al. (2011, 2018). (c-d) Single-grain glass shard compositions of Lake Chala visible and cryptotephra from Martin-Jones et al. (2020), Baxter et al. (2023) and this study.*

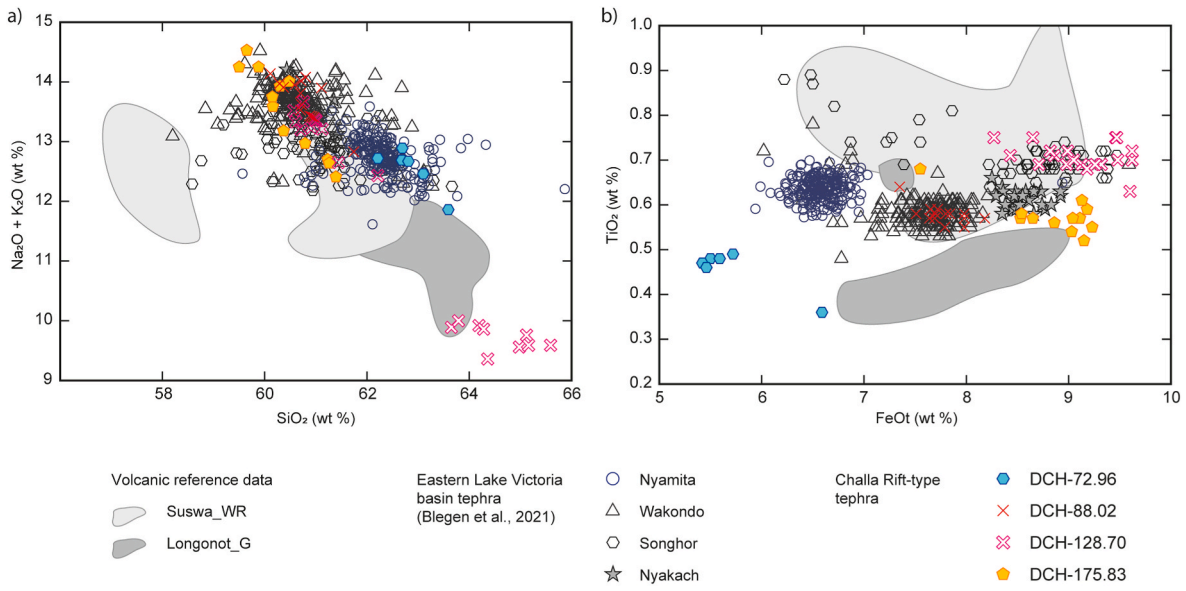

Fig. 6. *Major element biplot comparison between the glass compositions of CKR-type (low Al_2O_3/high FeOt) Lake Chala tephras with those of four >50 ka BP tuffs found widespread across the ELVB (Blegen et al., 2021), as well as reference envelopes of compositional data from CKR volcanoes Suswa (WR: whole rock) and Longonot (G: pumice glass) (Scott and Skilling, 1999; White et al., 2012). (a) Total alkali silica diagram; (b) FeOt (wt %) vs TiO_2 (wt %), which effectively distinguishes between the four DCH tephra layers.*

for which no geochemical or chronological data is available. Additional fieldwork is needed to evaluate whether these sources may have produced ash that reached Lake Chala.

3.4.2. Correlation to tephra of central Kenyan Rift volcanoes deposited in the eastern Lake Victoria basin

Lake Chala tephras DCH-72.96, DCH-88.02, DCH-128.70 and DCH-175.83 have trachyphonolite compositions plotting closely alongside the compositions of tephras erupted from Longonot, Suswa and Menengai in the CKR (Fig. 5), all of which have been active during the last 200 ka (Scott and Skilling, 1999; White et al., 2012). Most published compositional data on CKR volcanoes have been generated from whole rock analyses. Single-grain glass data are now available for tephra layers with wide distribution in Middle to Late Pleistocene sedimentary sequences in the ELVB. Although most of these likely derive from CKR volcanoes (Blegen et al., 2015, 2021), at present the 36-ka BP Menengai Tuff is the only regional trachyphonolite tephra younger than ~265 ka BP which has been securely correlated to its source, the Menengai caldera (Blegen et al., 2016).

In Fig. 6 we compare the glass composition of DCH-72.96, DCH-88.02, DCH-128.70 and DCH-175.83 with that of four of the most widespread trachyphonolitic tuffs reported by Blegen et al. (2021) from the ELVB, and which pre-date ~50 ka BP. To ensure comparability of the data, only tephra samples from Blegen et al. (2021)'s LVP18 collection that were analysed on the University of Cambridge WDS-EPMA instrument (i.e., in identical conditions as the Lake Chala tephra analyses) are plotted. Based on comparison of the respective major and minor elemental compositions, and with support from independent chronostratigraphic information, we propose two correlations between Lake Chala and the ELVB tephras.

Firstly, based on overlap of major and minor element compositions (Fig. 6), we correlate DCH-88.02 (here dated to 100.12–95.66 ka BP) to the Wakondo Tuff, first described by Tryon et al. (2010) from outcrops on Rusinga Island in Lake Victoria, and since then found throughout the ELVB including a host of sites in the Nyanza Rift (Blegen et al., 2015, 2021; Blegen, 2017). Tryon et al. (2010) and Blegen et al. (2021) tentatively associate the Wakondo Tuff to an eruption of either Longonot or Suswa, noting a K–Ar date of 100 ± 10 ka BP for the lowermost post-caldera phonolites at Suswa (Baker et al., 1988) that aligns with two U–Th dates of 111.4 ± 4.2 ka BP and 94.0 ± 3.3 ka BP on spring-fed fluvial tufa deposits incorporating the Wakondo Tuff at the Nyamtia site (Beverly et al., 2015).

Secondly, we establish a tentative correlation between DCH-128.70 (156.15–151.05 ka BP) and the Songhor Tuff, which is found ~3–5 m below the Wakondo Tuff at multiple outcropping geoarchaeological sequences in the ELVB (Blegen et al., 2015, 2021). DCH-128.70 glass has a bimodal major and minor element composition, of which the main mode with low SiO_2 and high Na_2O wt % overlaps closely with the main cluster of glass shards recovered from three samples of the Songhor Tuff (Fig. 6). The Songhor Tuff has not been dated directly, however stratigraphic control offered by the overlying Wakondo Tuff supports our correlation to DCH-128.70. As the Songhor Tuff composition matches only one of the two compositional modes present in DCH-128.70, we surmise that the missing compositional mode may not have been transported westward from potential source volcanoes in the CKR, whereas it did towards Lake Chala located to their southeast. Alternatively, the high SiO_2/low Na_2O wt % mode of DCH-128.70 may represent compositional variation due to Na loss during eruption, post-burial diagenesis, or geochemical analysis affecting approximately half of the analysed glass shards.

Compositional similarities are also observed between DCH-175.83 (215.32–213.52 ka BP) and the Nyakach Tuff presently recognised at two ELVB sites (Blegen et al., 2021), where it lies stratigraphically beneath the Wakondo and Songhor tuffs but no further chronological control is available. Although similar in most major and minor elements, their distinctive FeOt wt % values (Fig. 6) suggest that DCH-175.83 and the Nyakach Tuff may originate from temporally closely spaced explosive eruptions by the same source volcano.

The chemical signature of DCH-72.96 appears similar to DCH-88.02, DCH-128.70 and DCH-175.83 and the correlated ELVB tephras (Fig. 6), indicating a common origin in the CKR. However, as it does not match on all elements with any of the tephras in the Blegen et al. (2021) dataset, we cannot trace it to a previously known isochron at this time.

Finally, considering the compositional similarity between DCH-72.96, DCH-88.02, DCH-128.70, DCH-175.83 and their ELVB correlatives on the one hand, and whole rock data on <0.4 Ma BP pumices from Longonot (Scott and Skilling, 1999) and lava from Suswa (White et al., 2012) on the other (Fig. 6), we suggest that detailed glass geochemical

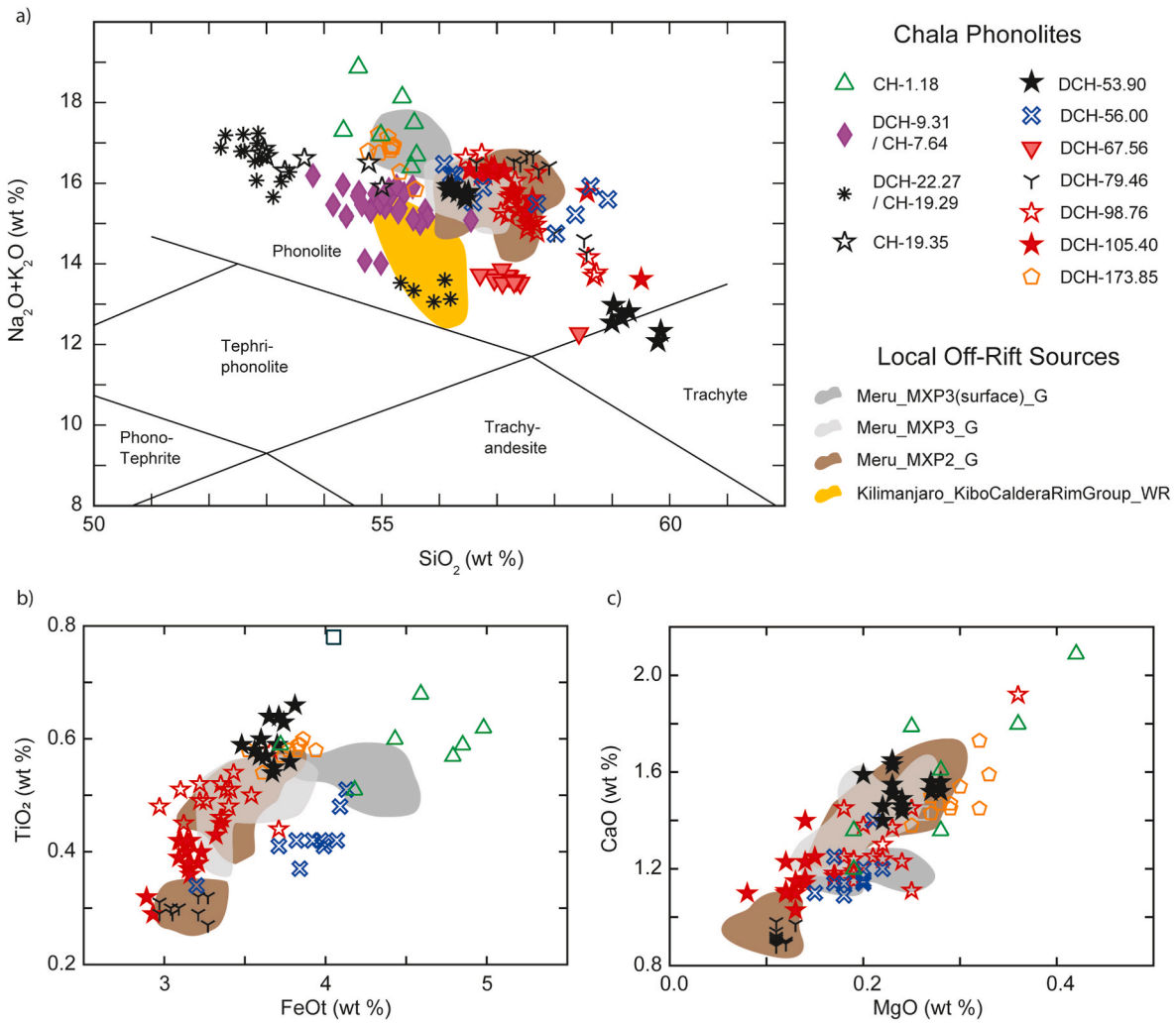

Fig. 7. Major and minor element biplots comparing the composition of all 15 phonolitic tephras from Lake Chala with compositional data from eruptions of Mt. Kilimanjaro's Kibo summit caldera (whole-rock data from Nonnotte et al., 2011) and Mt. Meru (new glass shard data for buried MXP2 and MXP3 pumices reported by Kisaka et al. (2021) and a surface pumice-lapilli associated with uppermost MXP3). (a) Total alkali-silica plot showing that only CH-1.18, DCH-53.90, DCH-56.00 mode a (Table 3), DCH-79.46, DCH-98.76, DCH-105.40 and DCH-173.85 overlap with the Mt. Meru pumice compositions. (b–c) Major-element comparison between these seven Lake Chala tephra and Mt. Meru reference data (compositional envelopes drawn by hand after outlier removal). Complete datasets are presented in Tables S9–10.

analyses of pyroclastic sequences from these CKR volcanoes might reveal the exact source of the far travelled ashes recorded in Lake Chala and the ELVB.

3.4.3. *Correlations to the nearby off-rift volcanoes Mt. Kilimanjaro and Mt. Meru*

Fig. 7 compares the glass major and minor element composition of the 11 phonolitic tephra, found throughout the Lake Chala sequence, with compositional envelopes of phonolitic eruptions from nearby Mt. Kilimanjaro and from Mt. Meru ~100 km to the west.

The most recent phonolitic explosive phase of Mt. Kilimanjaro's central summit Kibo has been K/Ar dated to between 200 and 150 ka BP (Nonnotte et al., 2011), putting it within the age range of the Deep-CHALLA sediment sequence. The only compositional data for Kibo vent eruptions available at present are mean values of whole-rock analyses on lava samples (Nonnotte et al., 2011), preventing precise comparison with the compositions of phonolite tephra from Lake Chala. However, assuming that these glass shard compositions will be equally or more evolved than counterpart whole-rock compositions, eruptions of the Kibo caldera are a feasible source for the oldest Lake Chala phonolites: DCH-98.76 (117.85–112.32 ka BP), DCH-105.40 (126.60–124.34 ka BP) and DCH-173.85 (213.77–210.32 ka BP).

As previously no single-grain glass data were available for Mt. Meru, we obtained single-grain glass data on pumice lapilli from the two youngest of the three buried fall deposits studied by Kisaka et al. (2021), termed MXP2 and MXP3, sampled on the western slopes of Mt. Meru. In addition, we add data from a grab sample of surficial pumice lapilli collected from the same area in 2014 (A. Delcamp pers. comm., 2012.), where pyroclastic deposits associated with the uppermost pyroclastic unit of MXP3 mantle the landscape. This sample may contain material from younger ashfall events (sample details in Table S9). Based on ^{14}C dating of palaeosols underlying MXP2 and MXP3 at three locations, Kisaka et al. (2021) report ages between ~39 and ~23 ka BP. However, these age estimates are ambiguous because the palaeosol dates are inconsistent between sequences, suggesting that some may be affected by unseen incorporation of young or old carbon. For now, we consider these deposits as potential correlatives of any of the pre-Holocene Lake Chala tephras with comparable compositions.

The pumice samples from Mt. Meru analysed in this study have phonolitic compositions, in agreement with the older whole-rock data which show that Mt. Meru typically erupts silica-undersaturated magmas (foidites, basanites through to phonolites; Roberts, 2003).

Major and minor element compositions of seven of the Lake Chala phonolite tephras (CH1.18, DCH-53.90, DCH-56.00, DCH-79.46, DCH-98.76, DCH-105.40 and DCH-173.85) overlap with those of pyroclastic materials sampled from Mt. Meru. On a total alkali-silica biplot (Fig. 7a), Mt. Meru pumice data form three clusters, however bi-plots of other elements (Fig. 7b and c) reveal that MXP2 has a bimodal composition and MXP3 overlaps on most elements with the lower silica mode of MXP2. The younger surface pumice sample is compositionally distinct from the two older pumice deposits by having slightly lower SiO_2 and higher FeOt (Table S9).

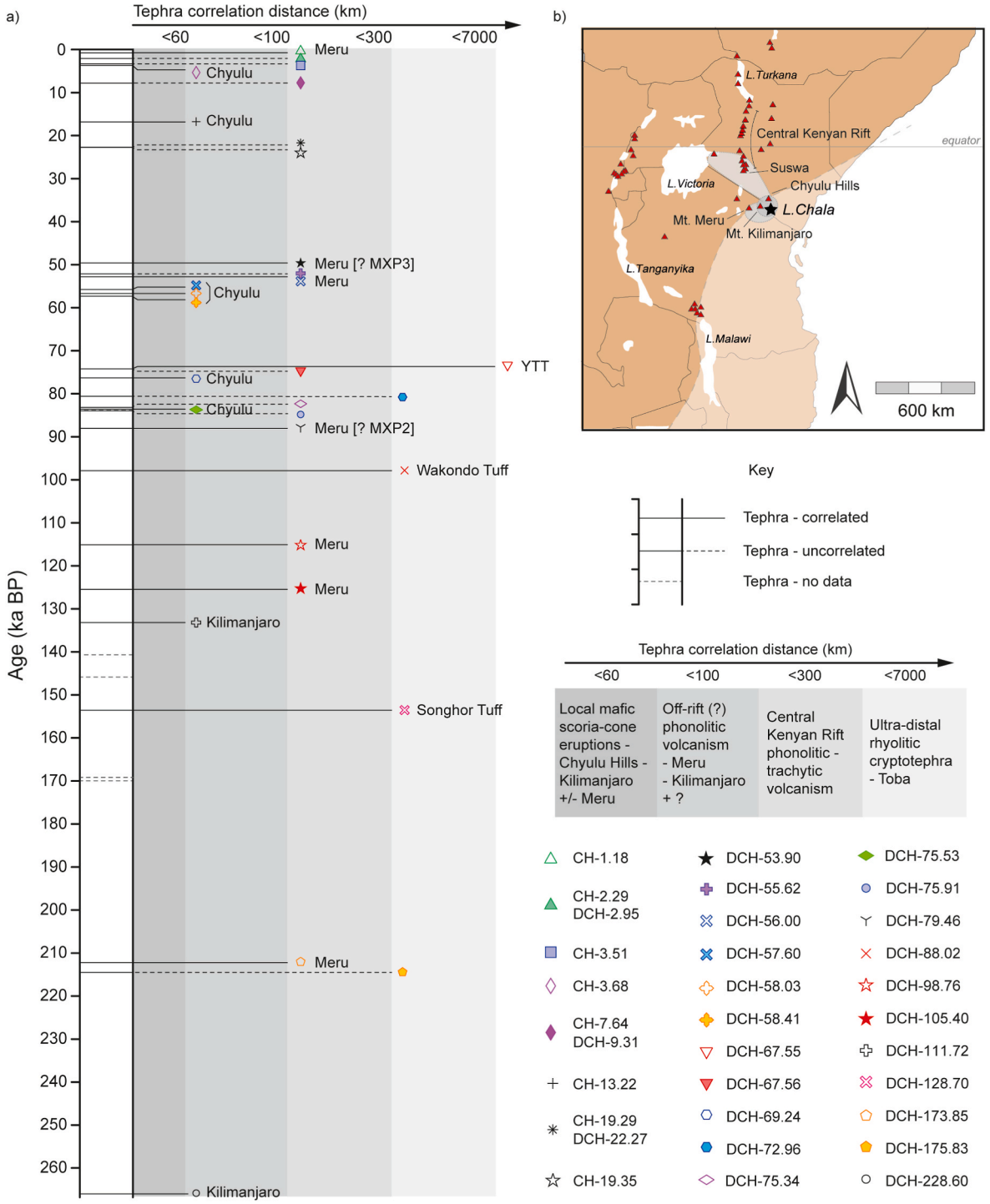

Fig. 8. (a) Lake Chala tephrostratigraphy showing the sequence of visible and detected cryptotephras, plotted according to the DCH_TephraAge timescale developed in this study. Horizontal line length and shaded zones indicate the approximate distance over which a tephra is believed to have been transported, i.e. the distance from Lake Chala to the correlated volcano (solid lines) or suggested source region (dashed lines) and the nature of the volcanism represented by those tephra. Symbols relate to the geochemical data in Figs. 5–7. Dashed lines limited to the stratigraphic column indicate tephra layers where limited EPMA data prevent attempts at correlation. (b) Overview map of eastern equatorial Africa with Holocene volcanoes (Global Volcanism Program, 2023) and major lake basins relative to the location of Lake Chala. Proposed volcanic sources for Lake Chala tephra, in Kenya and northern Tanzania, are labelled. Shaded envelopes indicate areas within which locally, regionally and extra-regionally defined tephra layers found in Lake Chala can be correlated, with the largest white envelope indicating the known YTT dispersal.

Relatively large scatter in compositional data of the Mt. Meru-like Lake Chala tephras, particularly in concentrations of alkali elements, likely relates to accidental partial analysis of crystal inclusions (microlites), observed in each of these tephras under the microscope (Table 1). Nevertheless, close similarity in all elements is observed between DCH-79.46 (90.25–86.98 ka BP) and the high SiO_2 mode of MXP2, the oldest of the Mt. Meru pumices. Similarly, the main glass shard cluster of DCH-53.90 (50.98–48.42 ka BP) shows close correspondence to the lower SiO_2 mode of MXP2 and is indistinguishable from MX3P. As the stratigraphic relationships between the two pairs of Lake Chala tephra and Mt. Meru pumice agree, this compositional correlation indicates that the two Mt. Meru pumices may be significantly older than suggested by the palaeosol ^{14}C dates published by Kisaka et al. (2021). The youngest phonolitic Lake Chala tephra, CH-1.18 (0.74–0.45 ka BP) shows closest resemblance to the surface pumice lapilli sample (Fig. 7), differing mainly on FeOt, TiO_2 and K_2O. We do not propose a correlation here but note that the most recent activity at Mt. Meru is producing less evolved (lower SiO_2) glass compositions than the other Mt. Meru-type tephra in the Lake Chala record, and can therefore not be correlated with MXP2 or MXP3.

In summary, at present we are unable to make firm correlations between individual phonolitic Lake Chala tephra layers and explosive eruptions of Mt. Kilimanjaro or Mt. Meru. However, based on compositional similarity we infer that Mt. Meru has been infrequently active during the last ~250 krs and that seven of these eruptions were voluminous enough to deposit visible ash layers in the bottom sediments of Lake Chala ~100 km to the east.

3.4.4. The Younger Toba Tuff at Lake Chala

As demonstrated by Baxter et al. (2023) and shown in Fig. 5, the composition of Lake Chala cryptotephra DCH-67.55 closely matches the high-silica distal YTT glasses found in India and Malaysia (Smith et al., 2011; Pearce et al., 2020) and YTT cryptotephra occurrences in other parts of Africa (Lane et al., 2013; Smith et al., 2018).

3.4.5. Uncorrelated tephra

Fig. 8 shows the temporal correlations made in this study between Lake Chala tephra and tephra from diverse volcanic source regions, individual volcanoes and eruption events. At present, 19 of the 35 documented Lake Chala tephra and cryptotephra are assigned to a source volcano, and likely source regions (transport distances) are suggested for another 11 (Fig. 8). Some of the uncorrelated tephra occur closely in time and can be grouped by composition (Fig. 5). For example, DCH-2.95/CH-2.29 (2.27–1.85 ka BP) and CH-3.51 (3.90–3.17 ka BP) were deposited within a ~1500-year period, suggesting that they likely represent tephra from sequential eruptions of the same but as yet unknown source volcano. The origin of some Lake Chala tephra layers remains elusive because they largely consist of clusters of minerals with thin glass selvedges (e.g., DCH-75.63 and DCH-75.91; Fig. 2, Table 1), rendering isolation of pure glass analyte under the 10-μm electron beam difficult, and causing accidental inclusion of crystals in the analysed area resulting in compositional outliers (Table S9). Discriminating crystal contamination from magmatic differentiation in tephra compositional data is challenging (Alloway et al., 2017), especially in small datasets of tephra with unknown composition.

The presence of crystals >500 μm length in many of the unassigned Lake Chala tephra layers (Table 1), both alongside and within glass shards, implies that these deposits most probably derive from eruptions relatively close to Lake Chala, as dense particles tend to fall out of suspension earlier than glass and are not normally transported 100s of kilometres (Fisher and Schmincke, 1984). Potential sources of the unassigned tephra layers may therefore be situated in poorly studied volcanic centres of the CKR or in northern Tanzania. For example, while Menengai and Longonot in the southern part of the CKR have erupted only trachytes, the most southerly volcano, Suswa, erupted phonolitic to trachytic compositions (Scott and Skilling, 1999; Macdonald, 2002; White et al., 2012; Blegen et al., 2016). Dates on Suswa lavas and tuffs show it was active between ~240 and 100 ka (White et al., 2012), when many Lake Chala tephras were deposited (Table 3). Until glass compositional data securely tied to Suswa are available, no firm correlations can be established. Even less compositional and chronological data is available for Middle to Late Pleistocene eruptions of volcanoes in northern Tanzania, although useful overviews have been compiled by Dawson (2008) and Mana et al. (2015). Located 200 km to the west-northwest of Lake Chala, Ol Doinyo Lengai is a source of pre-Holocene phonolitic tephra (Klaudius and Keller, 2006; Dawson, 2008; Mana et al., 2015) that could potentially have reached Lake Chala. Whole-rock data on Pleistocene-age Ol Doinyo Lengai lava samples (Fig. 5) so far do not suggest a compositional match to any of the Lake Chala tephra.

4. Discussion: a tephrostratotype record for eastern Africa

Our present inventory of 35 tephra layers sourced from volcanic centres within and beyond the EARS establishes the uninterrupted >250-kyr Lake Chala sediment record as a regional tephrostratotype sequence for eastern equatorial Africa. Based on geochemical compositions of glass shards, correlations could be made between a subset of the Lake Chala tephras and tephra layers documented from diverse geoarchaeological, palaeoenvironmental and volcanological settings throughout eastern Africa. In turn those sequences are assured to benefit from the added chronostratigraphic information and palaeoenvironmental context that may be transferred from the Lake Chala sequence.

4.1. An absolute chronology for the complete Lake Chala sediment record

Ten of the Lake Chala tephra contained sufficiently large and numerous sanidine crystals to allow direct $^{40}Ar/^{39}Ar$ dating, and these ages form the backbone of a first absolutely dated chronology for the complete 214.8-m long DeepCHALLA sequence presented here (Fig. 4). The present age-depth model describes a relatively constant linear rate of sediment accumulation in the Chala crater basin throughout its >250-kyr history, supporting seismic-stratigraphic and lithostratigraphic evidence for depositional continuity throughout lake history and demonstrating generally stable offshore sedimentation dynamics notwithstanding the seismic-stratigraphic evidence for significant changes in basin morphology and major lake-level fluctuation (Moernaut et al., 2010; Maitituerdi et al., 2022; Maitituerdi, 2023).

The chronology of the last 25 kyr is particularly well-constrained, by virtue of very precise transfer of the high-resolution 25-kyr CHALLACEA chronology (Blaauw et al., 2011), made possible by robust cross-correlation of predominantly mm-scale sediment lamination shared by both cored sequences. The much longer lower portion of the DeepCHALLA sequence is now supported by nine absolutely dated depth intervals (the YTT and eight directly Ar/Ar dated tephra layers). Overall, the age-depth relationship over this interval is highly coherent, testifying to an unusually stable rate of sediment accumulation throughout lake history with possible exception of somewhat accelerating sedimentation in the last ~50 kyr (Fig. 4). The four $^{40}Ar/^{39}Ar$ ages on Lake Chala tephras with analytical uncertainties exceeding 2.0 kyr are either fully consistent with adjacent intervals of which the age is better constrained, or partly (but never entirely) bypassed by the age model. The relatively well constrained $^{40}Ar/^{39}Ar$ age of DCH-67.56 (77.01 ± 0.93 ka BP) is also largely bypassed because of its proximity to cryptotephra DCH-67.55 which Baxter et al. (2023) identified as the 73.7 ± 0.6 ka BP YTT. Located only 1.5 cm below YTT in finely laminated organic lake muds, its $^{40}Ar/^{39}Ar$ age as measured in this study must be interpreted as inaccurate, despite an apparently robust single coherent juvenile crystal population (Table S7). An age difference of 3.31 ± 1.23 kyr (2σ) between two depth intervals that must have been deposited within only a few decades from each other (~25 years, based on long-term mean

accumulation) would imply a significant reduction in sedimentation rate, while there is no lithostratigraphic evidence for any change or hiatus in deepwater lacustrine deposition. Due to the small sample volume obtained from this visible but very thin (1 mm) tephra layer, we have no remaining sample to replicate and further investigate the cause of this age discrepancy. The modelled, and preferred, age of DCH-67.56 is 75.12-73.18 ka BP (Table 3).

The direction of age extrapolation beyond the lowermost absolutely dated depth interval (215.32–213.52 ka BP at DCH-175.83) proposed by DCH_TephraAge appears acceptable, as it extends backwards the linear rate of sediment accumulation which has been nearly perfectly constant for the period of ~165 kyr that follows (Fig. 4). However, this simple linear extrapolation must be considered provisional. Indeed the base of the drilled Lake Chala record is likely younger than ~266 ka BP, because of the likelihood of substantially higher linear sedimentation rates in the earliest phase of lake history (Depositional Stage I; Maitituerdi et al., 2022), when the lake-floor area available for lacustrine deposition was markedly smaller than today (cf. Davis and Ford, 1982; Håkanson and Jansson, 1983) such that clastic sediment influx per unit depositional area of this steep-sided crater catchment was higher than later on. Using isodepth maps of the rocky basement in Chala crater to quantify the change in lake-floor area through Stage I, Maitituerdi et al. (2022) found that proportional upward adjustment of sedimentation rates in the lowermost 44 m of the sequence (equivalent to the lowermost ~35 mefd) would yield a basal age up to ~20 kyr younger than when based on linear extrapolation of the long-term mean accumulation rate. The analysis of Maitituerdi et al. (2022) is based on seismic stratigraphy of the complete sedimentary column (i.e., with all event deposits included), therefore quantitative incorporation of their results into the age-depth model must await a complete coupling between core stratigraphy and seismic stratigraphy. Here we consider the DCH_TephraAge basal age of 266 ± 7 ka BP as maximum feasible age of the DeepCHALLA record, with a value of >250 ka BP being a more correct characterisation.

Modelled age estimates for most tephra layers in the DeepCHALLA sequence have uncertainties <4% (2RSD) and can be considered robust, yet there remains potential for further refinement. For example, $^{40}Ar/^{39}Ar$ dating of proximal tephra outcrops, where larger crystals and in greater volume may be preserved, at source volcanoes firmly correlated to Lake Chala tephras through glass composition analysis, would provide additional and improved tephra ages. Future work toward a multi-chronometer age model for the DeepCHALLA record (e.g., Roberts et al., 2021; Valero-Garcés et al., 2019) can also be expected to provide greater accuracy and robustness to the absolute chronology supporting the exceptional palaeoenvironmental archive contained in Lake Chala's sediments.

4.2. Connecting regional palaeoenvironmental and archaeological records

Tephra layers deposited by explosive volcanic eruptions within the EARS have long played a key role in dating and correlating archaeological sequences across eastern Africa (e.g., Blegen et al., 2018; Feibel, 1999; McHenry et al., 2008), and are increasingly being used to add chronological control to terrestrial and lacustrine palaeoenvironmental records (Lane et al., 2013, 2018; Deino et al., 2021; Roberts et al., 2021). However, absolutely dated tephras of Middle to Late Pleistocene age in this region remain rare, and only few pre-Holocene sequences contain more than a handful of tephra layers in stratigraphic order (e.g., Barker et al., 2003; Blegen et al., 2021; Deino et al., 2021). The Lake Chala tephrostratigraphy therefore provides an important framework for future correlation and dating of palaeoenvironmental and archaeological sequences. Its potential for correlating between regional archaeological sequences is demonstrated by our identification of four trachytic Lake Chala tephras that appear to originate from volcanoes within the CKR. Two of these CKR-type tephras (DCH-88.02 and DCH-128.70) correlate to the Wakondo and Songhor tuffs (Fig. 6) found in and around archaeological and palaeontological sites on the eastern shores of Lake Victoria, >200 km to the west of Lake Chala (Blegen et al., 2021). As such our DCH_Tephra age model (Fig. 3) provides the thus-far most robust age estimates for these important regional time markers, namely 100.12–95.66 ka BP for the Wakondo Tuff and 156.15–151.05 ka BP for the Songhor Tuff (Fig. 8, Table 3).

In addition, the Wakondo Tuff correlate DCH-88.02 occurs in sediments deposited during a pronounced low-stand phase of Lake Chala during Marine Isotope Stage (MIS) 5 (Moernaut et al., 2010; Maitituerdi et al., 2022), and may therefore provide a key stratigraphic marker for testing the regional synchroneity of the so-called 'MIS5 African megadroughts' (Cohen et al., 2007; Scholz et al., 2007), registered in several eastern African lake archives. These episodes of apparent hyper-aridity were first evidenced by reconstruction of extreme lake-level drops in the large Rift lakes Malawi and Tanganyika, but after discovery of the YTT in the Lake Malawi sediment record (Lane et al., 2013), the age model for that record has been adjusted differently by different authors (Ivory et al., 2016; Lyons et al., 2015), thus complicating the regional integration of Lake Malawi palaeoenvironmental proxy data. Episodes of low lake level within the same general timeframe have also been reported from Lake Naivasha in central Kenya (Trauth et al., 2003), and from palaeolake Chew Bahir (Schaebitz et al., 2021) and Lake Tana (Lamb et al., 2018) in Ethiopia, but available absolute dates on all these lake records do not suffice to determine whether the recorded events were (broadly) co-eval, or even how many of them deserve to be recognised as 'megadrought'.

Scholz et al. (2007) hypothesised that establishment of relatively stable humid conditions after the megadrought intervals (i.e., during MIS 4) provided suitable conditions for the dispersal of modern humans beyond the African continent. Although the narrative of modern human evolution and distribution within and beyond Africa has evolved since then (Groucutt et al., 2015; Scerri et al., 2018; Bergström et al., 2021), a common chronological marker layer that can directly relate the archaeological record to regional hydroclimate reconstructions would certainly promote understanding of climate-human-environment interaction during the Late Pleistocene.

4.3. The Younger Toba Tuff in Lake Chala

Tephra from the 73.7 ka BP (Mark et al., 2014, 2017) eruption of Mt. Toba in Sumatra, Indonesia, travelled nearly 7000 km west before falling out and being preserved as a cryptotephra layer in the Lake Chala sediment record Baxter et al. (2023). YTT glass shards are concentrated in a 0.5-cm-thick (~6-year) section of the DeepCHALLA sequence, with just a short upward tail (Fig. S3), providing a precisely pin-pointed time marker for incorporation in the DCH_TephraAge model (Fig. 4).

Atmospheric aerosol forcing caused by the YTT eruption has been hypothesised to have driven a severe volcanic winter (Robock et al., 2009), and even to have triggered abrupt global cooling at the onset of Greenland Stadial 20 (GS-20 at ~74 GICC05 ka BP; Rasmussen et al., 2014). Presumed extreme climate conditions have also been implicated in a possible genetic bottleneck of ancient modern humans in Africa (Ambrose, 1998). These ideas are countered by the apparent persistence of modern human populations (and their associated technologies) after the YTT eruption observed at archaeological sites in India and South Africa containing airfall deposits of the YTT (Petraglia et al., 2007; Smith et al., 2018). Also, sub-decadal-scale palaeoecological analysis of sediments below and above the YTT cryptotephra layer in Lake Malawi failed to detect evidence for unusual climatic variability (Lane et al., 2013; Jackson et al., 2015; Yost et al., 2018) at that time. Climate model simulations suggest that a climatic perturbation in the form of reduced global temperatures (estimates range from ~ 2 to 4 °C) and precipitation would have lasted less than five years (Timmreck et al., 2012; Black et al., 2021). Results of regionally resolved models differ dependent on background conditions and assigned forcing parameters. Using an offline dynamic vegetation model, Timmreck et al. (2012) inferred

expansion of grasslands over an interval lasting about a decade in areas of eastern and southern Africa occupied by modern humans. In contrast, Black et al. (2021) suggest that temperature and precipitation changes were likely muted. In any case, such a short-lived phenomenon would be hard to detect in most sedimentary records, where sample resolution is sub-decadal at best (e.g., Jackson et al., 2015; Yost et al., 2018). Moreover, even if a sub-decadal-scale perturbation is detected it cannot be precisely associated with the YTT if the isochron itself is not present in the same sequence. The discovery of the YTT in the Lake Chala record Baxter et al. (2023) constitutes the fourth observation in Africa, an important step in tracing this deposit across the expanding network of palaeoenvironmental and archaeological archives from the African continent. In the case of Lake Chala, the YTT isochron is contained within a palaeoenvironmental record that may be studied with seasonal to annual resolution. Further analysis of the DeepCHALLA sediment section bracketing the YTT isochron may therefore allow robust assessment of the YTT super-eruption's impacts on eastern Africa.

4.4. Reconstructing regional and local histories of volcanic eruptions

The volcanoes of eastern Africa are among the least well studied worldwide. According to the database approximately half of Holocene volcanoes in Kenya and Tanzania have no recorded pre-Holocene eruptions; and the LaMeve database of large (Magnitude >4) Quaternary eruptions (Crosweller et al., 2012) lists only 18 dated eruptions from the East African region. Tephra layers preserved in high-resolution continuous lake-sediment records such as that of Lake Chala represent a detailed catalogue of explosive volcanic eruptions which can be intermeshed with the volcanic stratigraphy in terrestrial contexts to track the occurrence and nature of past volcanism over long time scales. Our characterisation and dating of 35 tephras in the >250-kyr DeepCHALLA sequence thus provides a chronostratigraphic framework within which the number, sequence and timing of regional explosive volcanic eruptions may be compiled.

Lake Chala sediments have captured tephra from both frequently occurring, relatively local eruptions, and from highly explosive voluminous eruptions from volcanoes further afield. For example, we identified seven visible tephra layers deposited in the last ~213-kyr that are all likely to have derived from Mt. Meru ~100 km to the west of Lake Chala (Figs. 1, 6 and 8), interspersed with tephra from the CKR, some of which can be correlated to sites in the ELVB ~450 km away (Blegen et al., 2015, 2021). While the exact source volcanoes for many Lake Chala tephra layers are as yet unknown, the sequence of mafic tephras in the Lake Chala record revealed information about the frequency and products of scoria cone eruptions on the slopes of nearby Mt. Kilimanjaro and in the Chyulu Hills ~60 km away (Martin-Jones et al., 2020). Scoria cones are local basaltic pyroclastic deposits that typically reflect relatively low-volume Strombolian-style eruptions (Heiken, 1978), and in tropical environments they are susceptible to rapid subaerial weathering. However, as highlighted by Martin-Jones et al. (2020), preservation at Lake Chala of tephra from scoria cone eruptions in the Chyulu Hills supports evidence from other localities suggesting that even low-magnitude eruptions can produce distinctive chronostratigraphic markers in the regional geologic record (Luhr et al., 1993; Fontijn et al., 2016; Poppe et al., 2016). Secure age control on the eruptive histories of Mt. Kilimanjaro, Chyulu Hills and Mt. Meru and greater glass compositional datasets, including glass shard trace element compositions on proximal pyroclastic units and suspected distal correlatives, would allow further exploration of the correlations indicated in this study. However, in the case of both Mt. Meru and Chyulu Hills, the number of eruptions now identified and dated through study of the continuous Lake Chala sequence is greater than those recorded and dated through studies of the proximal volcanic stratigraphy (Wilkinson et al., 1986; Haug and Strecker, 1995; Späth et al., 2000; Roberts, 2003; Kisaka et al., 2021). Further cryptotephra analysis of the DeepCHALLA record will no doubt only reveal more.

4.5. Further development of the Lake Chala tephra record

Currently the sources for many Lake Chala tephras remain unknown, owing in part to lack of comparative compositional data on many EARS volcanoes. Although whole rock data provide a useful reference for a given volcano, individual eruptions are more difficult to discriminate particularly since many EARS volcanoes erupt glasses bracketing multiple compositional fields (Fig. 5). Our tephra correlations indicate that future fieldwork, dating and tephra studies should target Menengai, Suswa and Longonot in the CKR, and the volcanic centres to the south of Ol Doinyo Lengai, Mt. Meru and Mt. Kilimanjaro in northern Tanzania. Glass data, including trace elements, on proximal deposits may prove fruitful in determining the often-subtle geochemical distinctions between individual volcanoes, and between their sequential eruptions.

Many Lake Chala tephras have high crystal contents, preserving both free crystals and microlites within glass shards or selvedges (Table S1), and this merits further investigation to better understand the magmatic processes involved in the evolution and eruption of each volcanic event, besides helping to further constrain tephra correlations. Phenocrysts have already been used to fingerprint and correlate tephras erupted from Ol Doinyo Lengai and Ngorongoro in northern Tanzania (McHenry et al., 2008; Balashova et al., 2016, 2018), hence such a study on the Lake Chala tephras may constrain the correlation to their source.

5. Conclusions

Tephrostratigraphy of the ~250-kyr Lake Chala sediment sequence provides an important framework for tephra-isochron correlation of palaeoenvironmental, archaeological and eruption-history records throughout eastern equatorial Africa. Although not all 35 Lake Chala tephra layers identified to date can be correlated to their source volcano with presently available data, our current database of over 600 glass-shard analyses will enable future studies to characterize, date and correlate widely distributed tephra layers from EARS volcanoes in Kenya and Tanzania. The value of Lake Chala's tephrostratigraphic record will grow through time as additional correlations are made to tephra in newly studied volcanic outcrops and sediment sequences across the region, and as the DeepCHALLA sequence itself reveals more cryptotephra layers. Indeed, the six cryptotephras identified by this study are no doubt only a small subset of the entire cryptotephra inventory to be revealed by the DeepCHALLA sequence, underlining the at present highly incomplete nature of eastern Africa's known volcanic record.

Author contributions

Catherine Martin-Jones and **Christine Lane**: Conceptualisation, Methodology, Investigation, Formal analysis, Writing – original draft preparation, Visualisation (+**CL**: Funding acquisition). **Maarten Blaauw** and **Darren Mark**: Methodology, Formal analysis **Dirk Verschuren:** Conceptualisation, Resources, Funding acquisition. **Thijs Van der Meeren** and **Maarten Van Daele:** Formal analysis. **Hannah Wynton:** Visualisation. **Nick Blegen** and **Mary Kisaka:** Resources and Validation. **Melanie Leng** and **Phil Barker:** Conceptualisation, Funding acquisition. **All authors:** Writing- Reviewing and Editing.

Declaration of competing interest

The authors declare that they have no known competing financial interests or personal relationships that could have appeared to influence the work reported in this paper.

Data availability

Data is provided in the manuscript and SI files.

Acknowledgements

This research was funded jointly by a UK Natural Environment Research Council standard grant (NE/P011969/1) to CSL, a Ghent University Collaborative Research Operation grant (BOF13/GOA/023) to DV, and by the International Continental Scientific Drilling Program (ICDP) and diverse commingled financing from multiple scientific partners of the DeepCHALLA project (https://www.icdp-online.org/projects/world/africa/lake-challa-kenya-tanzania/). The authors thank the wider DeepCHALLA science team for their contributions and discussion of ideas, and the Continental Scientific Drilling (CSD) Facility, at the University of Minnesota (Minneapolis, USA) for facilitating the initial splitting, non-destructive scanning, photographing and description of the DeepCHALLA cores. Tephra analyses on the DeepCHALLA and CHALLACEA sequences were carried out in the Cambridge Tephra Laboratory within the Department of Geography Science Laboratories at the University of Cambridge, following pilot work on the CHALLACEA sequence undertaken in the Research Laboratory for Archaeology and the History of Art, University of Oxford as part of a Leverhulme Trust Early Career Fellowship to CSL. We thank Alma Piermattei and Friederike Murach-Ward for assisting with cryptotephra analysis on the CHALLACEA record. We are grateful to Audrey DelCamp (Vrije Universiteit Brussel) for providing a valuable recent tephra sample from Mt. Meru and Karen Fontijn (Université Libre de Bruxelles) for advice and comments on an early version of this paper. We also thank Iris Buisman (University of Cambridge) and Victoria Smith (University of Oxford) for supporting EPMA analyses. Finally, the authors thank the two anonymous referees for their constructive advice on improving the manuscript.

Appendix A. Supplementary data

Supplementary data to this article can be found online at https://doi.org/10.1016/j.quascirev.2023.108476.

References

Alloway, B.V., Moreno, P.I., Pearce, N.J.G., De Pol-Holz, R., Henríquez, W.I., Pesce, O.H., Sagredo, E., Villarosa, G., Outes, V., 2017. Stratigraphy, age and correlation of Lepué Tephra: a widespread c. 11 000 cal a BP marker horizon sourced from the Chaitén Sector of southern Chile. J. Quat. Sci. 32, 795–829.

Ambrose, S.H., 1998. Late Pleistocene human population bottlenecks, volcanic winter, and differentiation of modern humans. J. Hum. Evol. 34, 623–651.

Baker, B.H., 1987. Outline of the petrology of the Kenya rift alkaline province. Geological Society, London, Special Publications 30, 293–311.

Baker, B.H., 1967. Geology of the mount Kenya area. Geological Survey of Kenya Report 79, 464–465.

Baker, B.H., Mitchell, J.G., Williams, L.A.J., 1988. Stratigraphy, geochronology and volcano-tectonic evolution of the kedong–naivasha–kinangop region, gregory Rift valley, Kenya. J. Geol. Soc. 145, 107–116.

Balashova, A., Mattsson, H.B., Hirt, A.M., 2018. New tephrostratigraphic data from Lake Emakat (northern Tanzania): implications for the eruptive history of the Oldoinyo Lengai volcano. J. Afr. Earth Sci. 147, 374–382.

Balashova, A., Mattsson, H.B., Hirt, A.M., Almqvist, B.S.G., 2016. The Lake Natron Footprint Tuff (northern Tanzania): volcanic source, depositional processes and age constraints from field relations. J. Quat. Sci. 31, 526–537.

Barker, P., Williamson, D., Gasse, F., Gibert, E., 2003. Climatic and volcanic forcing revealed in a 50,000-year diatom record from Lake Massoko, Tanzania. Quaternary Research 60, 368–376. https://doi.org/10.1016/j.yqres.2003.07.001.

Barker, P.A., Hurrell, E.R., Leng, M.J., Wolff, C., Cocquyt, C., Sloane, H.J., Verschuren, D., 2011. Seasonality in equatorial climate over the past 25 ky revealed by oxygen isotope records from Mount Kilimanjaro. Geology 39, 1111–1114.

Baxter, A.J., Verschuren, D., Peterse, F., Miralles, D.G., Martin-Jones, C.M., Maitituerdi, A., Van der Meeren, T., Van Daele, M., Lane, C.S., Haug, G.H., Olago, D. O., Sinninghe Damsté, J.S., 2023. Reversed Holocene temperature–moisture relationship in the horn of Africa. Nature 620, 336–343.

Bell, K., Dawson, J.B., 1995. Nd and Sr isotope systematics of the active carbonatite volcano, Oldoinyo Lengai. In: Carbonatite Volcanism. Springer, pp. 100–112.

Bergström, A., Stringer, C., Hajdinjak, M., Scerri, E.M.L., Skoglund, P., 2021. Origins of modern human ancestry. Nature 590, 229–237.

Beverly, E.J., Driese, S.G., Peppe, D.J., Johnson, C.R., Michel, L.A., Faith, J.T., Tryon, C. A., Sharp, W.D., 2015. Recurrent spring-fed rivers in a Middle to Late Pleistocene semi-arid grassland: implications for environments of early humans in the Lake Victoria Basin, Kenya. Sedimentology 62, 1611–1635.

Biggs, J., Anthony, E.Y., Ebinger, C.J., 2009. Multiple inflation and deflation events at Kenyan volcanoes, East African Rift. Geology 37, 979–982.

Biggs, J., Bastow, I.D., Keir, D., Lewi, E., 2011. Pulses of deformation reveal frequently recurring shallow magmatic activity beneath the Main Ethiopian Rift. G-cubed 12.

Blaauw, M., Christen, J.A., 2011. Flexible paleoclimate age-depth models using an autoregressive gamma process. Bayesian analysis 6, 457–474.

Blaauw, M., van Geel, B., Kristen, I., Plessen, B., Lyaruu, A., Engstrom, D.R., van der Plicht, J., Verschuren, D., 2011. High-resolution 14C dating of a 25,000-year lake-sediment record from equatorial East Africa. Quat. Sci. Rev. 30, 3043–3059.

Black, B.A., Lamarque, J.-F., Marsh, D.R., Schmidt, A., Bardeen, C.G., 2021. Global climate disruption and regional climate shelters after the Toba supereruption. Proc. Natl. Acad. Sci. USA 118, e2013046118.

Blegen, N., 2017. The earliest long-distance obsidian transport: evidence from the~ 200 ka Middle stone age sibilo school road site, Baringo, Kenya. J. Hum. Evol. 103, 1–19.

Blegen, N., Brown, F.H., Jicha, B.R., Binetti, K.M., Faith, J.T., Ferraro, J.V., Gathogo, P. N., Richardson, J.L., Tryon, C.A., 2016. The Menengai Tuff: a 36 ka widespread tephra and its chronological relevance to Late Pleistocene human evolution in East Africa. Quat. Sci. Rev. 152, 152–168.

Blegen, N., Faith, J.T., Peppe, D.J., 2021. Tephrostratigraphy of the eastern Lake Victoria Basin including the Nyanza Rift, Kenya: building a stratigraphic and chronological framework for modern human evolution. Quat. Sci. Rev. 256, 106823 https://doi.org/10.1016/j.quascirev.2021.106823.

Blegen, N., Jicha, B.R., McBrearty, S., 2018. A new tephrochronology for early diverse stone tool technologies and long-distance raw material transport in the Middle to Late Pleistocene Kapthurin Formation, East Africa. J. Hum. Evol. 121, 75–103.

Blegen, N., Tryon, C.A., Faith, J.T., Peppe, D.J., Beverly, E.J., Li, B., Jacobs, Z., 2015. Distal tephras of the eastern Lake Victoria basin, equatorial East Africa: correlations, chronology and a context for early modern humans. Quat. Sci. Rev. 122, 89–111.

Blockley, S.P.E., Pyne-O'Donnell, S.D.F., Lowe, J.J., Matthews, I.P., Stone, A., Pollard, A. M., Turney, C.S.M., Molyneux, E.G., 2005. A new and less destructive laboratory procedure for the physical separation of distal glass tephra shards from sediments. Quat. Sci. Rev. 24, 1952–1960.

Bodé, S., De Wispelaere, L., Hemp, A., Verschuren, D., Boeckx, P., 2020. Water-isotope ecohydrology of mount Kilimanjaro. Ecohydrology 13, e2171.

Bolton, M.S.M., Jensen, B.J.L., Wallace, K., Praet, N., Fortin, D., Kaufman, D., De Batist, M., 2020. Machine learning classifiers for attributing tephra to source volcanoes: an evaluation of methods for Alaska tephras. J. Quat. Sci. 35, 81–92.

Brown, F.H., Fuller, C.R., 2008. Stratigraphy and tephra of the kibish formation, southwestern Ethiopia. J. Hum. Evol. 55, 366–403.

Brown, F.H., Nash, B.P., Fernandez, D.P., Merrick, H.V., Thomas, R.J., 2013. Geochemical composition of source obsidians from Kenya. J. Archaeol. Sci. 40, 3233–3251.

Brown, F.H., Sarna-Wojcicki, A.M., Meyer, C.E., Haileab, B., 1992. Correlation of Pliocene and Pleistocene tephra layers between the turkana basin of east Africa and the gulf of aden. Quat. Int. 13, 55–67.

Buckles, L.K., Verschuren, D., Weijers, J.W.H., Cocquyt, C., Blaauw, M., Sinninghe Damsté, J.S., 2016. Interannual and (multi-) decadal variability in the sedimentary BIT index of Lake Challa, East Africa, over the past 2200 years: assessment of the precipitation proxy. Clim. Past 12, 1243–1262.

Buckles, L.K., Weijers, J.W.H., Verschuren, D., Damsté, J.S.S., 2014. Sources of core and intact branched tetraether membrane lipids in the lacustrine environment: anatomy of Lake Challa and its catchment, equatorial East Africa. Geochem. Cosmochim. Acta 140, 106–126.

Calais, E., d'Oreye, N., Albaric, J., Deschamps, A., Delvaux, D., Déverchere, J., Ebinger, C., Ferdinand, R.W., Kervyn, F., Macheyeki, A.S., 2008. Strain accommodation by slow slip and dyking in a youthful continental rift, East Africa. Nature 456, 783–787.

Cohen, A.S., Stone, J.R., Beuning, K.R.M., Park, L.E., Reinthal, P.N., Dettman, D., Scholz, C.A., Johnson, T.C., King, J.W., Talbot, M.R., 2007. Ecological consequences of early Late Pleistocene megadroughts in tropical Africa. Proc. Natl. Acad. Sci. USA 104, 16422–16427.

Crosweller, H.S., Arora, B., Brown, S.K., Cottrell, E., Deligne, N.I., Guerrero, N.O., Hobbs, L., Kiyosugi, K., Loughlin, S.C., Lowndes, J., Nayembil, M., Siebert, L., Sparks, R.S.J., Takarada, S., Venzke, E., 2012. Global database on large magnitude explosive volcanic eruptions (LaMEVE). Journal of Applied Volcanology 1, 4. https://doi.org/10.1186/2191-5040-1-4.

Damsté, J.S.S., Ossebaar, J., Schouten, S., Verschuren, D., 2012. Distribution of tetraether lipids in the 25-ka sedimentary record of Lake Challa: extracting reliable TEX86 and MBT/CBT palaeotemperatures from an equatorial African lake. Quat. Sci. Rev. 50, 43–54.

Damsté, J.S.S., Verschuren, D., Ossebaar, J., Blokker, J., van Houten, R., van der Meer, M.T.J., Plessen, B., Schouten, S., 2011. A 25,000-year record of climate-induced changes in lowland vegetation of eastern equatorial Africa revealed by the stable carbon-isotopic composition of fossil plant leaf waxes. Earth Planet Sci. Lett. 302, 236–246.

Davies, L.J., Jensen, B.J.L., Froese, D.G., Wallace, K.L., 2016. Late Pleistocene and Holocene tephrostratigraphy of interior Alaska and Yukon: key beds and chronologies over the past 30,000 years. Quat. Sci. Rev. 146, 28–53. https://doi.org/10.1016/j.quascirev.2016.05.026.

Davies, S.M., 2015. Cryptotephras: the revolution in correlation and precision dating. J. Quat. Sci. 30, 114–130.

Davis, M.B., Ford, M.S., 1982. Sediment focusing in mirror lake, New Hampshire 1. Limnol. Oceanogr. 27, 137–150.

Dawson, J.B., 2008. The Gregory Rift Valley and Neogene-Recent Volcanoes of Northern Tanzania. Geological Society of London.

Dawson, J.B., Keller, J., Nyamweru, C., 1995. Historic and recent eruptive activity of Oldoinyo Lengai. In: Carbonatite Volcanism. Springer, pp. 4–22.
Dawson, J.B., Powell, D.G., 1969. The Natron-Engaruka explosion crater area, northern Tanzania. Bull. Volcanol. 33, 791–817.
Deino, A.L., Heil Jr., C., King, J., McHenry, L.J., Stanistreet, I.G., Stollhofen, H., Njau, J. K., Mwankunda, J., Schick, K.D., Toth, N., 2021. Chronostratigraphy and age modeling of Pleistocene drill cores from the Olduvai basin, Tanzania (Olduvai Gorge coring project). Palaeogeogr. Palaeoclimatol. Palaeoecol. 571, 109990.
Delcamp, A., Kervyn, M., Benbakkar, M., Kwelwa, S., Peter, D., 2017. Large volcanic landslide and debris avalanche deposit at Meru, Tanzania. Landslides 14, 833–847.
DiMaggio, E., Mana, S., Fontijn, K., 2021. East African Rift Tephra Database (EARThD) [WWW Document]. URL. https://sites.psu.edu/earthd/. accessed 9.28.21.
Dugmore, A., 1989. Icelandic volcanic ash in Scotland. Scot. Geogr. Mag. 105, 168–172.
Dunkley, P.N., Smith, M., Allen, D.J., Darling, W.G., 1993. The Geothermal Activity and Geology of the Northern Sector of the Kenya Rift Valley.
Feibel, C.S., 1999. Tephrostratigraphy and geological context in paleoanthropology. Evol. Anthropol. Issues News Rev. 8, 87–100.
Fisher, R.V., Schmincke, H.-U., 1984. Subaerial fallout tephra. In: Pyroclastic Rocks. Springer, pp. 125–162.
Fontijn, K., Ernst, G.G.J., Elburg, M.A., Williamson, D., Abdallah, E., Kwelwa, S., Mbede, E., Jacobs, P., 2010. Holocene explosive eruptions in the rungwe volcanic province, Tanzania. J. Volcanol. Geoth. Res. 196, 91–110. https://doi.org/10.1016/j.jvolgeores.2010.07.021.
Fontijn, K., McNamara, K., Tadesse, A.Z., Pyle, D.M., Dessalegn, F., Hutchison, W., Mather, T.A., Yirgu, G., 2018. Contrasting styles of post-caldera volcanism along the Main Ethiopian Rift: implications for contemporary volcanic hazards. J. Volcanol. Geoth. Res. 356, 90–113.
Fontijn, K., Rawson, H., Van Daele, M., Moernaut, J., Abarzúa, A.M., Heirman, K., Bertrand, S., Pyle, D.M., Mather, T.A., De Batist, M., 2016. Synchronisation of sedimentary records using tephra: a postglacial tephrochronological model for the Chilean Lake District. Quat. Sci. Rev. 137, 234–254.
Fontijn, K., Williamson, D., Mbede, E., Ernst, G.G.J., 2012. The Rungwe volcanic province, Tanzania–a volcanological review. J. Afr. Earth Sci. 63, 12–31.
Global Volcanism Program, 2023. Volcanoes of the World. https://doi.org/10.5479/si.GVP.VOTW5-2023.5.1 [WWW Document]. Distributed by Smithsonian Institution, compiled by Venzke, E accessed 8.4.23.
Groucutt, H.S., Petraglia, M.D., Bailey, G., Scerri, E.M.L., Parton, A., Clark-Balzan, L., Jennings, R.P., Lewis, L., Blinkhorn, J., Drake, N.A., 2015. Rethinking the dispersal of Homo sapiens out of Africa. Evol. Anthropol. Issues News Rev. 24, 149–164.
Håkanson, L., Jansson, M., 1983. Principles of Lake Sedimentology. Springer-verlag Berlin.
Haug, G.H., Strecker, M.R., 1995. Volcano-tectonic evolution of the Chyulu Hills and implications for the regional stress field in Kenya. Geology 23, 165–168.
Hay, R.L., 1989. Holocene carbonatite-nephelinite tephra deposits of Oldoinyo Lengai, Tanzania. J. Volcanol. Geoth. Res. 37, 77–91.
Heiken, G., 1978. Characteristics of tephra from cinder cone, Lassen volcanic national park, California. Bull. Volcanol. 41, 119–130.
Hogg, A.G., Heaton, T.J., Hua, Q., Palmer, J.G., Turney, C.S.M., Southon, J., Bayliss, A., Blackwell, P.G., Boswijk, G., Ramsey, C.B., 2020. SHCal20 Southern Hemisphere calibration, 0–55,000 years cal BP. Radiocarbon 62, 759–778.
Hutchison, W., Fusillo, R., Pyle, D.M., Mather, T.A., Blundy, J.D., Biggs, J., Yirgu, G., Cohen, B.E., Brooker, R.A., Barfod, D.N., Calvert, A.T., 2016. A pulse of mid-Pleistocene rift volcanism in Ethiopia at the dawn of modern humans. Nat. Commun. 7, 13192. http://www.nature.com/articles/ncomms13192#supplementary-information.
Ivory, S.J., Blome, M.W., King, J.W., McGlue, M.M., Cole, J.E., Cohen, A.S., 2016. Environmental change explains cichlid adaptive radiation at Lake Malawi over the past 1.2 million years. Proc. Natl. Acad. Sci. USA 113, 11895–11900.
Jackson, L.J., Stone, J.R., Cohen, A.S., Yost, C.L., 2015. High-resolution paleoecological records from Lake Malawi show no significant cooling associated with the Mount Toba supereruption at ca. 75 ka. Geology 43, 823–826.
Jensen, B.J.L., Pyne-O'Donnell, S., Plunkett, G., Froese, D.G., Hughes, P.D.M., Sigl, M., McConnell, J.R., Amesbury, M.J., Blackwell, P.G., van den Bogaard, C., Buck, C.E., Charman, D.J., Clague, J.J., Hall, V.A., Koch, J., Mackay, H., Mallon, G., McColl, L., Pilcher, J.R., 2014. Transatlantic distribution of the alaskan white river ash. Geology 42, 875–878. https://doi.org/10.1130/g35945.1.
Jochum, K.P., Nohl, U., Herwig, K., Lammel, E., Stoll, B., Hofmann, A.W., 2005. GeoReM: a new geochemical database for reference materials and isotopic standards. Geostand. Geoanal. Res. 29, 333–338.
Jochum, K.P., Stoll, B., Herwig, K., Willbold, M., Hofmann, A.W., Amini, M., Aarburg, S., Abouchami, W., Hellebrand, E., Mocek, B., 2006. MPI-DING reference glasses for in situ microanalysis: new reference values for element concentrations and isotope ratios. G-cubed 7.
Katoh, S., Nagaoka, S., WoldeGabriel, G., Renne, P., Snow, M.G., Beyene, Y., Suwa, G., 2000. Chronostratigraphy and correlation of the plio-pleistocene tephra layers of the Konso formation, southern main Ethiopian rift, Ethiopia. Quat. Sci. Rev. 19, 1305–1317.
Kisaka, M., Fontijn, K., Shemsanga, C., Tomašek, I., Gaduputi, S., Debaille, V., Delcamp, A., Kervyn, M., 2021. The late Quaternary eruptive history of Meru volcano, northern Tanzania. J. Volcanol. Geoth. Res. 417, 107314 https://doi.org/10.1016/j.jvolgeores.2021.107314.
Klaudius, J., Keller, J., 2006. Peralkaline silicate lavas at oldoinyo Lengai, Tanzania. Lithos 91, 173–190. https://doi.org/10.1016/j.lithos.2006.03.017.
Kristen, I., 2009. Investigations on Rainfall Variability during the Late Quaternary Based on Geochemical Analyses of Lake Sediments from Tropical and Subtropical Southern Africa. University of Potsdam, Potsdam (Germany).
Kuiper, K.F., Deino, A., Hilgen, F.J., Krijgsman, W., Renne, P.R., Wijbrans, J, R., 2008. Synchronizing rock clocks of Earth history. science 320, 500–504.
Lamb, H.F., Bates, C.R., Bryant, C.L., Davies, S.J., Huws, D.G., Marshall, M.H., Roberts, H.M., Toland, H., 2018. 150,000-year palaeoclimate record from northern Ethiopia supports early, multiple dispersals of modern humans from Africa. Sci. Rep. 8, 1077. https://doi.org/10.1038/s41598-018-19601-w.
Lane, C.S., Chorn, B.T., Johnson, T.C., 2013. Ash from the Toba supereruption in Lake Malawi shows no volcanic winter in East Africa at 75 ka. Proceedings of the National Academy of Sciences of the United States of America 110, 8025–8029. https://doi.org/10.1073/pnas.1301474110.
Lane, C.S., Cullen, V.L., White, D., Bramham-Law, C.W.F., Smith, V.C., 2014. Cryptotephra as a dating and correlation tool in archaeology. J. Archaeol. Sci. 42 https://doi.org/10.1016/j.jas.2013.10.033.
Lane, C.S., Lowe, D.J., Blockley, S.P.E., Suzuki, T., Smith, V.C., 2017. Advancing tephrochronology as a global dating tool: applications in volcanology, archaeology, and palaeoclimatic research. Quat. Geochronol. 40 https://doi.org/10.1016/j.quageo.2017.04.003.
Lane, C.S., Martin-Jones, C.M., Johnson, T.C., 2018. A cryptotephra record from the Lake Victoria sediment core record of holocene palaeoenvironmental change. Holocene 28. https://doi.org/10.1177/0959683618798163.
Le Bas, M.J.L.E., Maitre, R.W.L.E., Streckeisen, A., Zanettin, B., Rocks, I.S. on the S. of I, 1986. A chemical classification of volcanic rocks based on the total alkali-silica diagram. J. Petrol. 27, 745–750.
Lee, J.-Y., Marti, K., Severinghaus, J.P., Kawamura, K., Yoo, H.-S., Lee, J.B., Kim, J.S., 2006. A redetermination of the isotopic abundances of atmospheric Ar. Geochem. Cosmochim. Acta 70, 4507–4512.
Lowe, D.J., Pearce, N.J.G., Jorgensen, M.A., Kuehn, S.C., Tryon, C.A., Hayward, C.L., 2017. Correlating tephras and cryptotephras using glass compositional analyses and numerical and statistical methods: review and evaluation. Quat. Sci. Rev. 175, 1–44.
Lowe, J.J., Bronk Ramsey, C., Housley, R.A., Lane, C.S., Tomlinson, E.L., Stringer, C., Davies, W., Barton, N., Pollard, M., Gamble, C., Menzies, M., Rohling, E., Roberts, A., Blockley, S., Cullen, V., Grant, K., Lewis, M., MacLeod, A., White, D., Albert, P., Hardiman, M., Lee, S., Oh, A., Satow, C., Cross, J.K., Law, C.B., Todman, A., Bourne, A., Matthews, I., Müller, W., Smith, V., Wulf, S., Anghelinu, M., Antl-Weiser, W., Bar-Yosef, O., Boric, D., Boscato, P., Ronchitelli, A., Chabai, V., Veselsky, A., Uthmeier, T., Farrand, W., Gjipali, I., Ruka, R., Güleç, E., Karavanic, I., Karkanas, P., King, T., Komšo, D., Koumouzelis, M., Kyparissi, N., Lengyel, G., Mester, Z., Neruda, P., Panagopoulou, E., Shalamanov-Korobar, L., Tolevski, I., Sirakov, N., Guadelli, A., Guadelli, J.-L., Ferrier, C., Skrdla, P., Slimak, L., Soler, N., Soler, J., Soressi, M., Tushabramishvilii, N., Zilhão, J., Angelucci, D., Albert, P., Bramham Law, C., Cullen, V.L., Lincoln, P., Staff, R., Flower, K., Aouadi-Abdeljaouad, N., Belhouchet, L., Barker, G., Bouzouggar, A., Van Peer, P., Kindermann, K., Gerken, K., Niemann, H., Tipping, R., Saville, A., Ward, T., Clausen, I., Weber, M.-J., Kaiser, K., Torksdorf, J.F., Turner, F., Veil, S., Nygaard, N., Pyne-O'Donnell, S.D.F., Masojc, M., Nalepka, D., Jurochnik, A., Kabacinski, J., Antoine, P., Olive, M., Christensen, M., Bodu, P., Debout, G., Orliac, M., De Bie, M., Van Gils, M., Paulissen, E., Brou, L., Leesch, D., Hadorn, P., Thew, N., Riede, F., Heinen, M., Joris, O., Richter, J., Uthmeier, T., Knipping, M., Stika, H.-P., Friedrich, M., Conard, N., Malina, M., Kind, C.-J., Beutelspacher, T., Mortensen, M. F., Burdukiewicz, J.M., Szynkiewicz, A., Poltowicz-Bobak, M., Bobak, D., Wisniewski, A., Przezdziecki, M., Valde-Nowak, P., Muzyczuk, A., Bramham Law, C., Cullen, V.L., Davies, L., Lincoln, P., MacLeod, A., Morgan, P., Aydar, E., Çubukçu, E., Brown, R., Coltelli, M., Castro, D.L., Cioni, R., DeRosa, R., Donato, P., Roberto, A.D., Gertisser, R., Giordano, G., Branney, M., Jordan, N., Keller, J., Kinvig, H., Gottsman, J., Blundy, J., Marani, M., Orsi, G., Civetta, L., Arienzo, I., Carandente, A., Rosi, M., Zanchetta, G., Seghedi, I., Szakacs, A., Sulpizio, R., Thordarson, T., Trincardi, F., Vigliotti, L., Asioli, A., Piva, A., Andric, M., Brauer, A., de Klerk, P., Filippi, M.-L., Finsinger, W., Galovic, L., Jones, T., Lotter, A., Müller, U., Pross, J., Mangerud, J., Lohne, Ø., Pyne-O'Donnell, S., Markovic, S., Pini, R., Ravazzi, C., Riede, F., TheuerKauf, M., Tzedakis, C., Margari, V., Veres, D., Wastegård, S., Ortiz, J.E., Torres, T., Díaz-Bautista, A., Moreno, A., Valero-Garcés, B., Lowick, S., Ottolini, L., 2015. The RESET project: constructing a European tephra lattice for refined synchronisation of environmental and archaeological events during the last c. 100 ka. Quat. Sci. Rev. 118 https://doi.org/10.1016/j.quascirev.2015.04.006.
Luhr, J.F., Simkin, T., Cuasay, M., 1993. Parícutin: the Volcano Born in a Mexican Cornfield. US Geoscience Press.
Lyons, R.P., Scholz, C.A., Cohen, A.S., King, J.W., Brown, E.T., Ivory, S.J., Johnson, T.C., Deino, A.L., Reinthal, P.N., McGlue, M.M., 2015. Continuous 1.3-million-year record of East African hydroclimate, and implications for patterns of evolution and biodiversity. Proc. Natl. Acad. Sci. USA 112, 15568–15573.
Macdonald, R., 2002. Magmatism of the Kenya Rift valley: a review. Earth and Environmental Science Transactions of the Royal Society of Edinburgh 93, 239–253.
Macdonald, R., Davies, G.R., Bliss, C.M., Leat, P.T., Bailey, D.K., Smith, R.L., 1987. Geochemistry of high-silica peralkaline rhyolites, Naivasha, Kenya Rift valley. J. Petrol. 28, 979–1008.
Macdonald, R., Davies, G.R., Upton, B.G.J., Dunkley, P.N., Smith, M., Leat, P.T., 1995. Petrogenesis of Silali volcano, gregory rift, Kenya. J. Geol. Soc. 152, 703–720.
Macgregor, D., 2015. History of the development of the East African Rift System: a series of interpreted maps through time. J. Afr. Earth Sci. 101, 232–252.
Maitituerdi, A., 2023. Depositional History of Lake Chala (Mt. Kilimanjaro, Equatorial East Africa): Reference Frame for a High-Resolution, ~250-kyr Paleoenvironmental Archive. Unpublished PhD Thesis, University of Haifa (Israel).
Maitituerdi, A., Van Daele, M., Verschuren, D., De Batist, M., Waldmann, N., 2022. Depositional history of Lake Chala (Mt. Kilimanjaro, equatorial East Africa) from high-resolution seismic stratigraphy. J. Afr. Earth Sci., 104499

Mana, S., Furman, T., Turrin, B.D., Feigenson, M.D., Swisher, C.C., 2015. Magmatic activity across the East african north Tanzanian divergence zone. J. Geol. Soc. 172, 368–389.
Mark, D.F., Petraglia, M., Smith, V.C., Morgan, L.E., Barfod, D.N., Ellis, B.S., Pearce, N.J., Pal, J.N., Korisettar, R., 2014. A high-precision 40Ar/39Ar age for the Young Toba Tuff and dating of ultra-distal tephra: forcing of Quaternary climate and implications for hominin occupation of India. Quat. Geochronol. 21, 90–103. https://doi.org/10.1016/j.quageo.2012.12.004.
Mark, D.F., Renne, P.R., Dymock, R.C., Smith, V.C., Simon, J.I., Morgan, L.E., Staff, R.A., Ellis, B.S., Pearce, N.J.G., 2017. High-precision 40Ar/39Ar dating of Pleistocene tuffs and temporal anchoring of the Matuyama-Brunhes boundary. Quat. Geochronol. 39, 1–23.
Mark, D.F., Stuart, F.M., De Podesta, M., 2011. New high-precision measurements of the isotopic composition of atmospheric argon. Geochem. Cosmochim. Acta 75, 7494–7501.
Marshall, A.S., Macdonald, R., Rogers, N.W., Fitton, J.G., Tindle, A.G., Nejbert, K., Hinton, R.W., 2009. Fractionation of peralkaline silicic magmas: the greater olkaria volcanic complex, Kenya Rift Valley. J. Petrol. 50, 323–359.
Martin-Jones, C., Lane, C., Van Daele, M., Van der Meeren, T., Wolff, C., Moorhouse, H., Tomlinson, E., Verschuren, D., 2020. History of scoria-cone eruptions on the eastern shoulder of the Kenya–Tanzania Rift revealed in the 250-ka sediment record of Lake Chala near Mount Kilimanjaro. J. Quat. Sci. 35, 245–255.
Martin-Jones, C.M., Lane, C.S., Pearce, N.J.G., Smith, V.C., Lamb, H.F., Oppenheimer, C., Asrat, A., Schaebitz, F., 2017. Glass compositions and tempo of post-17 ka eruptions from the Afar Triangle recorded in sediments from lakes Ashenge and Hayk, Ethiopia. Quat. Geochronol. 37 https://doi.org/10.1016/j.quageo.2016.10.001.
McHenry, L.J., 2012. A revised stratigraphic framework for Olduvai Gorge Bed I based on tuff geochemistry. J. Hum. Evol. 63, 284–299.
McHenry, L.J., Mollel, G.F., Swisher, C.C., 2008. Compositional and textural correlations between Olduvai Gorge bed I tephra and volcanic sources in the Ngorongoro volcanic highlands, Tanzania. Quat. Int. 178, 306–319. https://doi.org/10.1016/j.quaint.2007.01.004.
McHenry, L.J., Stanistreet, I.G., 2018. Tephrochronology of bed II, Olduvai Gorge, Tanzania, and placement of the oldowan–acheulean transition. J. Hum. Evol. 120, 7–18. https://doi.org/10.1016/j.jhevol.2017.12.006.
McNamara, K., Cashman, K.V., Rust, A.C., Fontijn, K., Chalié, F., Tomlinson, E.L., Yirgu, G., 2018. Using lake sediment cores to improve records of volcanism at Aluto volcano in the main Ethiopian rift. G-cubed 19, 3164–3188.
Meyer, I., Van Daele, M., Fiers, G., Verleyen, E., De Batist, M., Verschuren, D., 2018. Sediment reflectance spectroscopy as a paleo-hydrological proxy in East Africa. Limnol Oceanogr. Methods 16, 92–105.
Mibei, G., Harðarson, B.S., Franzson, H., Bali, E., Geirsson, H., Guðfinnsson, G.H., 2021. Eruptive history and volcano-tectonic evolution of Paka volcanic complex in the northern Kenya rift: insights into the geothermal heat source. J. Afr. Earth Sci. 173, 103951 https://doi.org/10.1016/j.jafrearsci.2020.103951.
Moernaut, J., Verschuren, D., Charlet, F., Kristen, I., Fagot, M., De Batist, M., 2010. The seismic-stratigraphic record of lake-level fluctuations in Lake Challa: hydrological stability and change in equatorial East Africa over the last 140kyr. Earth Planet Sci. Lett. 290, 214–223. https://doi.org/10.1016/j.epsl.2009.12.023.
Nelson, D.M., Verschuren, D., Urban, M.A., Hu, F.S., 2012. Long-term variability and rainfall control of savanna fire regimes in equatorial East Africa. Global Change Biol. 18, 3160–3170.
Niespolo, E.M., Rutte, D., Deino, A.L., Renne, P.R., 2017. Intercalibration and age of the Alder Creek sanidine 40Ar/39Ar standard. Quat. Geochronol. 39, 205–213.
Nomade, S., Renne, P.R., Vogel, N., Deino, A.L., Sharp, W.D., Becker, T.A., Jaouni, A.R., Mundil, R., 2005. Alder Creek sanidine (ACs-2): a Quaternary 40Ar/39Ar dating standard tied to the Cobb Mountain geomagnetic event. Chem. Geol. 218, 315–338.
Nonnotte, P., Benoit, M., Le Gall, B., Hémond, C., Rolet, J., Cotten, J., Brunet, P., Makoba, E., 2011. Petrology and geochemistry of alkaline lava series, Kilimanjaro, Tanzania: new constraints on petrogenetic processes. Volcanism and Evolution of the African Lithosphere: Geol. Soc. Am. Spec. Pap. 478, 127–158.
Nonnotte, P., Guillou, H., Le Gall, B., Benoit, M., Cotten, J., Scaillet, S., 2008. New K–Ar age determinations of Kilimanjaro volcano in the North Tanzanian diverging rift, East Africa. J. Volcanol. Geoth. Res. 173, 99–112.
Olago, D.O., Street-Perrott, F.A., Perrott, R.A., Ivanovich, M., Harkness, D.D., 2000. Late quaternary primary tephras in sacred lake sediments, northeast mount Kenya, Kenya. J. Afr. Earth Sci. 30, 957–969.
Ortega-Guerrero, B., García, L.C., Linares-López, C., 2018. Tephrostratigraphy of the late quaternary record from Lake chalco, central méxico. J. S. Am. Earth Sci. 81, 122–140.
Pearce, N.J.G., Westgate, J.A., Gualda, G.A.R., Gatti, E., Muhammad, R.F., 2020. Tephra glass chemistry provides storage and discharge details of five magma reservoirs which fed the 75 ka Youngest Toba Tuff eruption, northern Sumatra. J. Quat. Sci. 35, 256–271.
Petraglia, M., Korisettar, R., Boivin, N., Clarkson, C., Ditchfield, P., Jones, S., Koshy, J., Lahr, M.M., Oppenheimer, C., Pyle, D., 2007. Middle Paleolithic assemblages from the Indian subcontinent before and after the Toba super-eruption. science 317, 114–116.
Pickford, M., Senut, B., Poupeau, G., Brown, F.H., Haileab, B., 1991. Correlation of tephra layers from the western Rift valley (Uganda) to the turkana basin (Ethiopia/Kenya) and the gulf of aden. Stratigraphy 313, 223–229.
Ponomareva, V., Portnyagin, M., Davies, S.M., 2015. Tephra without borders: far-reaching clues into past explosive eruptions. Front. Earth Sci. 3, 83.
Poppe, S., Smets, B., Fontijn, K., Rukeza, M.B., Migabo, A.D.M.F., Milungu, A.K., Namogo, D.B., Kervyn, F., Kervyn, M., 2016. Holocene phreatomagmatic eruptions alongside the densely populated northern shoreline of Lake Kivu, East African Rift: timing and hazard implications. Bull. Volcanol. 78, 82.
Pyle, D.M., 1999. Widely dispersed quaternary tephra in Africa. Global Planet. Change 21, 95–112.
Pyle, D.M., Ricketts, G.D., Margari, V., van Andel, T.H., Sinitsyn, A.A., Praslov, N.D., Lisitsyn, S., 2006. Wide dispersal and deposition of distal tephra during the Pleistocene 'Campanian Ignimbrite/Y5'eruption, Italy. Quat. Sci. Rev. 25, 2713–2728.
Rasmussen, S.O., Bigler, M., Blockley, S.P., Blunier, T., Buchardt, S.L., Clausen, H.B., Cvijanovic, I., Dahl-Jensen, D., Johnsen, S.J., Fischer, H., Gkinis, V., Guillevic, M., Hoek, W.Z., Lowe, J.J., Pedro, J.B., Popp, T., Seierstad, I.K., Steffensen, J.P., Svensson, A.M., Vallelonga, P., Vinther, B.M., Walker, M.J.C., Wheatley, J.J., Winstrup, M., 2014. A stratigraphic framework for abrupt climatic changes during the Last Glacial period based on three synchronized Greenland ice-core records: refining and extending the INTIMATE event stratigraphy. Quat. Sci. Rev. 106, 14–28. https://doi.org/10.1016/j.quascirev.2014.09.007.
Rawson, H., Naranjo, J.A., Smith, V.C., Fontijn, K., Pyle, D.M., Mather, T.A., Moreno, H., 2015. The frequency and magnitude of post-glacial explosive eruptions at Volcán Mocho-Choshuenco, southern Chile. J. Volcanol. Geoth. Res. 299, 103–129.
Reimer, P.J., Austin, W.E.N., Bard, E., Bayliss, A., Blackwell, P.G., Bronk Ramsey, C., Butzin, M., Cheng, H., Edwards, R.L., Friedrich, M., Grootes, P.M., Guilderson, T.P., Hajdas, I., Heaton, T.J., Hogg, A.G., Hughen, K.A., Kromer, B., Manning, S.W., Muscheler, R., Palmer, J.G., Pearson, C., van der Plicht, J., Reimer, R.W., Richards, D.A., Scott, E.M., Southon, J.R., Turney, C.S.M., Wacker, L., Adolphi, F., Büntgen, U., Capano, M., Fahrni, S.M., Fogtmann-Schulz, A., Friedrich, R., Köhler, P., Kudsk, S., Miyake, F., Olsen, J., Reinig, F., Sakamoto, M., Sookdeo, A., Talamo, S., 2020. The IntCal20 northern hemisphere radiocarbon age calibration curve (0–55 cal kBP). Radiocarbon 62, 725–757. https://doi.org/10.1017/RDC.2020.41.
Renne, P.R., Balco, G., Ludwig, K.R., Mundil, R., Min, K., 2011. Response to the comment by WH Schwarz et al. on "Joint determination of 40K decay constants and 40Ar*/40K for the Fish Canyon sanidine standard, and improved accuracy for 40Ar/39Ar geochronology" by PR Renne et al.(2010). Geochem. Cosmochim. Acta 75, 5097–5100.
Renne, P.R., Cassata, W.S., Morgan, L.E., 2009. The isotopic composition of atmospheric argon and 40Ar/39Ar geochronology: time for a change? Quat. Geochronol. 4, 288–298.
Renne, P.R., Mundil, R., Balco, G., Min, K., Ludwig, K.R., 2010. Joint determination of 40K decay constants and 40Ar*/40K for the Fish Canyon sanidine standard, and improved accuracy for 40Ar/39Ar geochronology. Geochem. Cosmochim. Acta 74, 5349–5367.
Renne, P.R., Norman, E.B., 2001. Determination of the half-life of 37 Ar by mass spectrometry. Phys. Rev. C 63, 47302.
Renne, P.R., Sharp, Z.D., Heizler, M.T., 2008. Cl-derived argon isotope production in the CLICIT facility of OSTR reactor and the effects of the Cl-correction in 40Ar/39Ar geochronology. Chem. Geol. 255, 463–466.
Richardson, J.L., Richardson, A.E., 1972. History of an African rift lake and its climatic implications. Ecol. Monogr. 42, 499–534.
Roberts, H.M., Ramsey, C.B., Chapot, M.S., Deino, A.L., Lane, C.S., Vidal, C., Asrat, A., Cohen, A., Foerster, V., Lamb, H.F., 2021. Using multiple chronometers to establish a long, directly-dated lacustrine record: constraining> 600,000 years of environmental change at Chew Bahir, Ethiopia. Quat. Sci. Rev. 266, 107025.
Roberts, M.A., 2003. Geochemical and Volcanological Evolution of the Mt. Meru Region, Northern Tanzania.
Robock, A., Ammann, C.M., Oman, L., Shindell, D., Levis, S., Stenchikov, G., 2009. Did the Toba volcanic eruption of~ 74 ka BP produce widespread glaciation? J. Geophys. Res. Atmos. 114.
Rogers, N.W., Evans, P.J., Blake, S., Scott, S.C., Hawkesworth, C.J., 2004. Rates and timescales of fractional crystallization from 238U–230Th–226Ra disequilibria in trachyte lavas from Longonot volcano, Kenya. J. Petrol. 45, 1747–1776.
Rose, W.I., Durant, A.J., 2009. Fine ash content of explosive eruptions. J. Volcanol. Geoth. Res. 186, 32–39. https://doi.org/10.1016/j.jvolgeores.2009.01.010.
Rosenthal, A., Foley, S.F., Pearson, D.G., Nowell, G.M., Tappe, S., 2009. Petrogenesis of strongly alkaline primitive volcanic rocks at the propagating tip of the western branch of the East African Rift. Earth Planet Sci. Lett. 284, 236–248.
Saggerson, E.P., 1963. Geology of the simba-kibwezi area. Geological Survey of Kenya 58, 70.
Scerri, E.M.L., Thomas, M.G., Manica, A., Gunz, P., Stock, J.T., Stringer, C., Grove, M., Groucutt, H.S., Timmermann, A., Rightmire, G.P., 2018. Did our species evolve in subdivided populations across Africa, and why does it matter? Trends Ecol. Evol. 33, 582–594.
Schaebitz, F., Asrat, A., Lamb, H.F., Cohen, A.S., Foerster, V., Duesing, W., Kaboth-Bahr, S., Opitz, S., Viehberg, F.A., Vogelsang, R., 2021. Hydroclimate changes in eastern Africa over the past 200,000 years may have influenced early human dispersal. Communications Earth & Environment 2, 1–10.
Scholz, C.A., Johnson, T.C., Cohen, A.S., King, J.W., Peck, J.A., Overpeck, J.T., Talbot, M.R., Brown, E.T., Kalindekafe, L., Amoako, P.Y.O., 2007. East African megadroughts between 135 and 75 thousand years ago and bearing on early-modern human origins. Proc. Natl. Acad. Sci. USA 104, 16416–16421.
Scott, S.C., Skilling, I.P., 1999. The role of tephrachronology in recognizing synchronous caldera-forming events at the Quaternary volcanoes Longonot and Suswa, south Kenya Rift. Geological Society, London, Special Publications 161, 47–67.
Shane, P., Westgate, J., Williams, M., Korisettar, R., 1995. New geochemical evidence for the youngest Toba tuff in India. Quaternary Research 44, 200–204.
Smith, E.I., Jacobs, Z., Johnsen, R., Ren, M., Fisher, E.C., Oestmo, S., Wilkins, J., Harris, J.A., Karkanas, P., Fitch, S., Ciravolo, A., Keenan, D., Cleghorn, N., Lane, C.S.,

Matthews, T., Marean, C.W., 2018. Humans thrived in South Africa through the Toba eruption about 74,000 years ago. Nature 555. https://doi.org/10.1038/nature25967.
Smith, V.C., Pearce, N.J.G., Matthews, N.E., Westgate, J.A., Petraglia, M.D., Haslam, M., Lane, C.S., Korisettar, R., Pal, J.N., 2011. Geochemical fingerprinting of the widespread Toba tephra using biotite compositions. Quat. Int. 246 https://doi.org/10.1016/j.quaint.2011.05.012.
Späth, A., Le Roex, A.P., Opiyo-Akech, N., 2001. Plume–lithosphere interaction and the origin of continental rift-related alkaline volcanism—the Chyulu Hills volcanic province, southern Kenya. J. Petrol. 42, 765–787.
Späth, A., Le Roex, A.P., Opiyo-Akech, N., 2000. The petrology of the Chyulu Hills volcanic province, southern Kenya. J. Afr. Earth Sci. 31, 337–358.
Stoenner, R.W., Schaeffer, O.A., Katcoff, S., 1965. Half-lives of argon-37, argon-39, and argon-42. Science 148, 1325–1328.
Swai, V., 2018. Lake Chala Statigraphy: Developing a Method to Identify and Quantify Surficial Slope Sediment Remobilization. Ghent University, Ghent (Belgium).
Tadesse, A.Z., Fontijn, K., Melaku, A.A., Gebru, E.F., Smith, V.C., Tomlinson, E., Barfod, D., Gopon, P., Bégué, F., Caricchi, L., 2022. Eruption frequency and magnitude in a geothermally active continental rift: the Bora-Baricha-Tullu Moye volcanic complex, Main Ethiopian Rift. J. Volcanol. Geoth. Res., 107471
Tadesse, A.Z., Fontijn, K., Melaku, A.A., Gebru, E.F., Smith, V.C., Tomlinson, E., Barfod, D., Gopon, P., Bégué, F., Caricchi, L., Laha, P., 2022. Eruption frequency and magnitude in a geothermally active continental rift: The Bora-Baricha-Tullu Moye volcanic complex, Main Ethiopian Rift. J. Volcanol. Geoth. Res. 423, 107471.
Thompson, A.O., Dodson, R.G., 1963. Geology of the Naivasha area. Geological Survey of Kenya Report 55, 1–80.
Timmreck, C., Graf, H.-F., Zanchettin, D., Hagemann, S., Kleinen, T., Krüger, K., 2012. Climate response to the Toba super-eruption: regional changes. Quat. Int. 258, 30–44.
Tomlinson, E.L., Smith, V.C., Albert, P.G., Aydar, E., Civetta, L., Cioni, R., Çubukçu, E., Gertisser, R., Isaia, R., Menzies, M.A., 2015. The major and trace element glass compositions of the productive Mediterranean volcanic sources: tools for correlating distal tephra layers in and around Europe. Quat. Sci. Rev. 118, 48–66.
Trauth, M.H., Deino, A.L., Bergner, A.G.N., Strecker, M.R., 2003. East African climate change and orbital forcing during the last 175 kyr BP. Earth Planet Sci. Lett. 206, 297–313.
Tryon, C.A., Faith, J.T., Peppe, D.J., Fox, D.L., McNulty, K.P., Jenkins, K., Dunsworth, H., Harcourt-Smith, W., 2010. The Pleistocene archaeology and environments of the wasiriya beds, Rusinga Island, Kenya. J. Hum. Evol. 59, 657–671.
Tryon, C.A., McBrearty, S., 2006. Tephrostratigraphy of the bedded tuff member (Kapthurin Formation, Kenya) and the nature of archaeological change in the later Middle Pleistocene. Quaternary Research 65, 492–507.
Tryon, C.A., McBrearty, S., 2002. Tephrostratigraphy and the acheulian to Middle stone age transition in the Kapthurin Formation, Kenya. J. Hum. Evol. 42, 211–235.
Tryon, C.A., Roach, N.T., Logan, M.A.V., 2008. The Middle Stone Age of the northern Kenyan Rift: age and context of new archaeological sites from the Kapedo Tuffs. J. Hum. Evol. 55, 652–664.
Turney, C.S.M., Harkness, D.D., Lowe, J.J., 1997. Rapid Communication: the use of microtephra horizons to correlate Late-glacial lake sediment successions in Scotland. J. Quat. Sci. 12, 525–531.
Valero-Garcés, B.L., González-Sampériz, P., Gil-Romera, G., Benito, B.M., Moreno, A., Oliva-Urcia, B., Aranbarri, J., García-Prieto, E., Frugone, M., Morellón, M., Arnold, L. J., Demuro, M., Hardiman, M., Blockley, S.P.E., Lane, C.S., 2019. A multi-dating approach to age-modelling long continental records: the 135 ka El Cañizar de Villarquemado sequence (NE Spain). Quat. Geochronol. 54 https://doi.org/10.1016/j.quageo.2019.101006.
Van Daele, M., Meyer, I., Moernaut, J., De Decker, S., Verschuren, D., De Batist, M., 2017. A revised classification and terminology for stacked and amalgamated turbidites in environments dominated by (hemi) pelagic sedimentation. Sediment. Geol. 357, 72–82.
van der Bilt, W.G.M., Lane, C.S., Bakke, J., 2017. Ultra-distal Kamchatkan ash on Arctic Svalbard: towards hemispheric cryptotephra correlation. Quat. Sci. Rev. 164 https://doi.org/10.1016/j.quascirev.2017.04.007.
van der Plas, G.W., Rucina, S.M., Hemp, A., Marchant, R.A., Hooghiemstra, H., Schüler, L., Verschuren, D., 2021. Climate-human-landscape interaction in the eastern foothills of Mt. Kilimanjaro (equatorial East Africa) during the last two millennia. Holocene 31, 556–569.
van Geel, B., Gelorini, V., Lyaruu, A., Aptroot, A., Rucina, S., Marchant, R., Damsté, J.S. S., Verschuren, D., 2011. Diversity and ecology of tropical African fungal spores from a 25,000-year palaeoenvironmental record in southeastern Kenya. Rev. Palaeobot. Palynol. 164, 174–190.
Vandergoes, M.J., Hogg, A.G., Lowe, D.J., Newnham, R.M., Denton, G.H., Southon, J., Barrell, D.J.A., Wilson, C.J.N., McGlone, M.S., Allan, A.S.R., 2013. A revised age for the Kawakawa/Oruanui tephra, a key marker for the Last Glacial Maximum in New Zealand. Quat. Sci. Rev. 74, 195–201.
Verschuren, D., Damsté, J.S.S., Moernaut, J., Kristen, I., Blaauw, M., Fagot, M., Haug, G. H., Challacea project members, 2009. Half-precessional dynamics of monsoon rainfall near the East African Equator. Nature 462, 637–641.
Verschuren, D., Olago, D.O., Rucina, S.M., Odhengo, P.O., 2013. DeepCHALLA: two glacial cycles of climate and ecosystem dynamics from equatorial East Africa. Sci. Drill. 15, 72–76.
Vidal, C.M., Lane, C.S., Asrat, A., Barfod, D.N., Mark, D.F., Tomlinson, E.L., Tadesse, A.Z., Yirgu, G., Deino, A., Hutchison, W., 2022. Age of the oldest known Homo sapiens from eastern Africa. Nature 1–5.
Weaver, S.D., 1977. The Quaternary caldera volcano Emuruangogolak, Kenya Rift, and the petrology of a bimodal ferrobasalt-pantelleritic trachyte association. Bull. Volcanol. 40, 209–230.
White, J.C., Espejel-García, V.V., Anthony, E.Y., Omenda, P., 2012. Open system evolution of peralkaline trachyte and phonolite from the Suswa volcano, Kenya rift. Lithos 152, 84–104.
Wilkinson, P., Mitchell, J.G., Cattermole, P.J., Downie, C., 1986. Volcanic chronology of the men–kilimanjaro region, northern Tanzania. J. Geol. Soc. 143, 601–605.
Williams, L.A.J., 1978. Character of Quaternary volcanism in the Gregory rift valley. Geological Society, London, Special Publications 6, 55–69.
WoldeGabriel, G., Hart, W.K., Katoh, S., Beyene, Y., Suwa, G., 2005. Correlation of Plio–Pleistocene Tephra in Ethiopian and Kenyan rift basins: temporal calibration of geological features and hominid fossil records. J. Volcanol. Geoth. Res. 147, 81–108.
Wolff, C., Haug, G.H., Timmermann, A., Damsté, J.S.S., Brauer, A., Sigman, D.M., Cane, M.A., Verschuren, D., 2011. Reduced interannual rainfall variability in East Africa during the last ice age. Science 333, 743–747.
Wolff, C., Kristen-Jenny, I., Schettler, G., Plessen, B., Meyer, H., Dulski, P., Naumann, R., Brauer, A., Verschuren, D., Haug, G.H., 2014. Modern seasonality in Lake Challa (Kenya/Tanzania) and its sedimentary documentation in recent lake sediments. Limnol. Oceanogr. 59, 1621–1636.
Wulf, S., Keller, J., Paterne, M., Mingram, J., Lauterbach, S., Opitz, S., Sottili, G., Giaccio, B., Albert, P.G., Satow, C., 2012. The 100–133 ka record of Italian explosive volcanism and revised tephrochronology of Lago Grande di Monticchio. Quat. Sci. Rev. 58, 104–123.
Wulf, S., Kraml, M., Brauer, A., Keller, J., Negendank, J.F.W., 2004. Tephrochronology of the 100 ka lacustrine sediment record of Lago Grande di Monticchio (southern Italy). Quat. Int. 122, 7–30.
Wulf, S., Kraml, M., Keller, J., 2008. Towards a detailed distal tephrostratigraphy in the Central Mediterranean: the last 20,000 yrs record of Lago Grande di Monticchio. J. Volcanol. Geoth. Res. 177, 118–132.
Yost, C.L., Jackson, L.J., Stone, J.R., Cohen, A.S., 2018. Subdecadal phytolith and charcoal records from Lake Malawi, East Africa imply minimal effects on human evolution from the~ 74 ka Toba supereruption. J. Hum. Evol. 116, 75–94.